CHARACTERIZATION OF PMN-35PT THIN FILM RELAXOR FERROELECTRIC

CHARACTERIZATION OF PMN-35PT THIN FILM RELAXOR FERROELECTRIC

BY

DECLAN KEOGH. B. ENG MGT.

A THESIS

SUBMITTED TO THE SCHOOL OF GRADUATE STUDIES

IN PARTIAL FULFILMENT OF THE REQUIREMENTS

FOR THE DEGREE

MASTER OF APPLIED SCIENCE

MCMASTER UNIVERSITY

MASTER OF APPLIED SCIENCE (2006) **MCMASTER UNIVERSITY**

(MATERIALS SCIENCE AND ENGINEERING) HAMILTON, ONTARIO

TITLE: CHARACTERIZATION OF PMN-35PT THIN FILM RELAXOR FERROELECTRICS

AUTHOR: DECLAN KEOGH, B. ENG. MGT.

SUPERVISOR: PROFESSOR: PROFESSOR GIANLUIGI A. BOTTON

NUMBER OF PAGES: viii, 82

Abstract

High quality epitaxial thin films of lead magnesium niobate – lead titanate (PMN-0.35PT) were deposited on $MgAl_2O_4$ substrates in the (001) direction with a lattice mismatch of less than 2%. Characterization by transmission electron microscopy and x-ray diffraction, has revealed high quality single crystal epitaxial thin films oriented in the (001) direction with a tetragonal unit cell. Capacitance measurements were completed by interdigital dielectrometry and using Finite Element Modeling the dielectric constant for the thin film yielded values ranging from 561 – 799 at 1kHz and 518 – 746 at 100kHz when the temperature was varied from 273-473K. Additionally, the dielectric maximum has been shifted to higher temperature and the frequency dispersion of the dielectric constant appears to be minimized.

Piezoresponse microscopy and transmission electron microscopy was completed on both single and multilayer heterostructures. Transmission electron microscopy shows that the single layer samples show excellent morphology with single crystal epitaxial growth in the (001) direction. In addition piezoresponse microscopy and TEM have elucidated the difficulty in producing high quality films of PMN-0.35PT with a $BaNb_{0.5}Ti_{0.5}0_3$ bottom electrode. The tendency for columnar growth of $BaNb_{0.5}Ti_{0.5}0_3$ establishes an environment for polycrystalline growth drastically reducing the probability of single crystal growth in subsequent layers. Finally, piezoresponse microscopy allowed the observation of self polarization in PMN-0.35PT within the polycrystalline films which is in agreement with observations of previous researchers.

Acknowledgement

The author wishes to express the most sincere thanks to professor Gianluigi A. Botton. His tireless commitment, encouragement and thoughtful discussion during this work both motivated and provided an excellent environment for academic research.

The author also wishes to thank all the helpful staff of The Brockhouse Institute for Materials Research specifically Dr. John Preston, Dr. Antoni Dabkowski, and Dr. Rob Hughes for their helpful discussion, expertise and the opportunity to complete the author's research. The author is also very grateful to Dr. Alain Pignolet and Catalin Harnagea of INRS in Varennes, QC and Dr. Jamal Deen and Dr. Ognian Marinov of ECE at McMaster University, for their experimental expertise and the opportunity to work with them at their prestigious facilities. Furthermore, the author would also like to thank all the students with which he had the pleasure of working with throughout this work.

Finally, the author wishes to thank his wonderful parents and sisters for their encouragement during this time and his loving girlfriend, Josie Vitulli, for her constant support and kind words during the many late nights and weekends that went into this project.

Table of Contents

Abstract iv
Acknowledgement v
Table of Contents vi
Table of Figures vii
1 Introduction 1
1.1 Introduction to Ferroelectric Materials and Devices 1
1.2 Objectives of Research 4
2 Literature Review of Relaxor Ferroelectrics and their Thin Films 5
2.1 Ferroelectric Crystals 5
2.1.1 Ferroelectric Physics 7
2.1.2 Ferroelectric Domains 11
2.1.3 Relaxor Ferroelectrics 14
2.1.4 Lead Magnesium Niobate-Lead Titanate 15
2.2 Dielectric Theory of Relaxor Ferroelectric 19
2.3 Pulsed Laser Deposition 21
2.4 Thin Film Effects in Ferroelectric Materials 23
2.5 Dielectric Characterization 25
2.5.1 Interdigital Capacitors 26
2.6 Capacitance Modeling 28
2.7 Piezoresponse Force Microscopy (PFM) 31
2.7.1 Principle of operation 32
3 Experimental Techniques 38
3.1 Thin Film Deposition 38
3.2 Lift off Photolithography 40
3.3 Transmission Electron Microscope Sample Preparation 42
3.4 Electronic Characterization Techniques 43
3.4.1 Electric Field Modeling 44
3.5 Piezoresponse Microscopy 49
4 Results and Discussion 51
4.1 Single Layer Samples 51
4.1.1 Electric Field and Capacitance Modeling 51
4.1.2 Dielectric Results 55
4.1.3 Microstructural Characterization 62
4.2 Multilayer Samples 66
4.2.1 Piezoelectric Response 66
4.2.2 Microstructural Characterization 72
5 Conclusions 76
5.1 Summary 76
5.2 Recommendations for Future Work 77
References 78

Table of Figures

Figure 1: Dielectric and frequency response of normal ferroelectrics and relaxor ferroelectrics....3

Figure 2: Interrelationship of ferroelectric and subgroups on the basis of symmetry....5

Figure 3: Schematic structure of a fictitious ferroelectric crystal....8

Figure 4: Schematic potential wells....8

Figure 5: Schematic Ferroelectric Hysteresis Loop....9

Figure 6: Sawyer Tower Circuit construction....10

Figure 7: Domain stability in thin films undergoing a cubic to tetragonal phase transition a) single and polydomain orientations b) Domain stability map....14

Figure 8: Hysteretic response of relaxor ferroelectric with increasing temperature....15

Figure 9: Structure of PMN-PT solid solution in cubic and tetragonal phase....16

Figure 10: Phase diagram of PMN-PT solid solution....17

Figure 11: Two-dimensional illustration of order-disorder in hypothetical Smolenskii model....20

Figure 12: Schematic of pulsed laser deposition chamber....21

Figure 13: Calculated phase diagram vs. misfit strain and associated dielectric constant versus misfit strain for (001) oriented epitaxial $BaTiO_3$....25

Figure 14: Top view of interdigital circuit design....26

Figure 15: Schematic depicting the bending of electric field lines from a flat plate to an IDC capacitor....27

Figure 16: Electric field lines between electrodes in a multilayer capacitor construction (Gevorgian)....30

Figure 17: Principle of PFM a) zero bias and no contrast b) positive bias applied to tip change in thickness c) opposite thickness changes with negative bias applied to tip33

Figure 18: Demodulation of polarization state information from the piezoresponse signal....35

Figure 19: Drawing of experimental heterostructures a)single layer sample b)multilayer heterostructure....39

Figure 20: Flowchart depicting experimental design and execution....44

Figure 21: Multilayer heterostructure mounted on a wafer with silver paste connection..50

Figure 22: 2D Electric field vectors for IDC structure as calculated by Maxwell....52

Figure 23 Dielectric constant versus capacitance for various dielectric thicknesses.....53
Figure 24: Maple output for thin dielectric layer.....54
Figure 25: Measured Capacitance of Substrate sample versus temperature.....55
Figure 26: Capacitance versus frequency with increasing temperature from 273 K to 423K.....57
Figure 27: Measured capacitance vs. temperature for frequencies 1kHz-100kHz (PMNT 45).....57
Figure 28: Dielectric constant of single crystal using Maxwell FEM extraction.....59
Figure 29: Dielectric constant of PMNT ceramic using Maxwell FEM extraction.....59
Figure 30: Dielectric constant of the sample PMNT 45 using Maxwell FEM extraction.60
Figure 31: Typical XRD Pattern of PMN-0.35PT on $MgAl_2O_4$ Substrate (PMNT14).....63
Figure 32: Bright Field TEM image of PMNT on $MgAl_2O_4$ substrate (PMNT27).....64
Figure 33: CBED pattern on the (100) ZA of (a) substrate (b) PMNT-0.35PT film.....65
Figure 34: Topographical AFM image of a) b) (001) and c) d) (111) oriented PMN-0.35PT.....68
Figure 35: AFM image of PMN-PT deposited in (001) orientation a)topography and b) is the associated piezoresponse image.....69
Figure 36: AFM image of PMN-PT deposited in (111) orientation a)topography and b) is the associated piezoresponse image.....70
Figure 37: SEM Micrograph of PMN-PT surface in a) (100) orientation and b) (111) orientation (Rob Hughes).....72
Figure 38: TEM cross-section of three layer heterostructure.....74
Figure 39: TEM Cross-section of PMN-0.35PT layer with associated CBED patterns....75

1 Introduction

1.1 Introduction to Ferroelectric Materials and Devices

Ferroelectric materials and devices have been widely used and investigated for a range of applications across many industries. Ferroelectric phenomena were first observed in the late 1800's in Rochelle Salt[1] however the discovery of barium titanate ceramics during World War II was the beginning of the materials widespread use. The unusually high dielectric constant of the material spawned a flurry of investigations into the source of the phenomena and alternative materials. With the increased interest numerous ferroelectric materials and new and interesting phenomena associated with ferroelectricity were also discovered.

Ferroelectric materials are now part of several multi-billion dollar industries including, ultrasonic transducers, radio and communication filters, pyroelectric security surveillance devices, medical diagnostic transducers, stereo tweeters, buzzers, gas igniters, positive temperature coefficient (PTC) sensors and switches, ultrasonic motors, electro-optic light valves, thin-film capacitors, and ferroelectric thin-film memories.[1]

Innovations and advances in microelectronics and microelectronic mechanical devices have been the driving force behind ferroelectric research over the past decade. The performance of devices based on ferroelectric materials is dependent on the important parameters of dielectric constant, dielectric loss, and piezoelectric or electrostrictive constants.

Currently the pervasive choice for high performance devices is ceramic $Pb(Zr_{1-x}Ti_x)O_3$. They are known to have anomalously high dielectric properties and electromechanical coupling, especially in the region of the morphotrophic phase boundary where both tetragonal and rhombohedral phases may coexist.[2] This is due to enhanced polarizability from coupling between equivalent energy states from the coexistent phases.[3] In typical PZT systems the relative dielectric constant can be as high as 3500, electromechanical coupling factor can approach 75%, and the piezoelectric coefficient can be as high as 590 pC/N. However, translating the superior properties of this material from ceramic into single crystal form has proven difficult as obtaining crystals of sufficient size has not been successful.

In light of the difficulties encountered with PZT, the development of other single crystal ferroelectrics with excellent properties have been thoroughly investigated in recent years. In particular, relaxor ferroelectrics, a subset of normal ferroelectrics have been developed in both single crystal and thin film form. First discovered by Smolenskii in the 1950s[4], relaxor ferroelectrics have proven to demonstrate the characteristics desired by industry, namely high dielectric constant, low dielectric loss and excellent electromechanical behavior. In addition, relaxor ferroelectrics have a frequency dispersive, broad dielectric maximum. This is in contrast to normal ferroelectrics which have a rapid onset and then more gradual reduction in dielectric maximum as shown in Figure 1

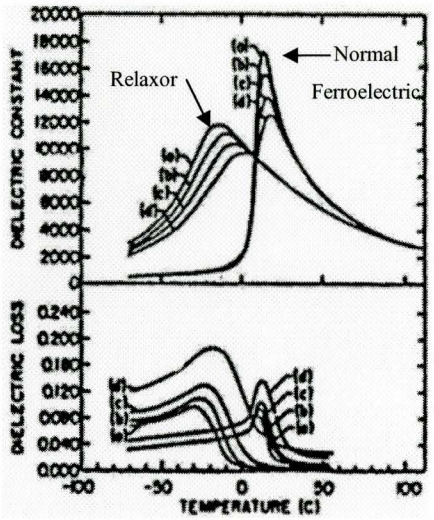

Figure 1: Dielectric and frequency response of normal ferroelectrics and relaxor ferroelectrics[5]

The thin film form of relaxor materials have shown great promise as they may be developed and implemented into existing applications where typically a single crystal material would be used. However, research has shown that inferior dielectric and electromechanical properties can be expected in polycrystalline films and there is very little literature related to single crystal thin films. It is speculated that the inferior properties are due to stress within the thin film due to lattice mismatch between the substrate and film, although, to date a study of the dielectric and electromechanical behavior of high quality relaxor films has not been completed.

Previous research within the group has developed well oriented (001) single crystal thin films of $0.65Pb(Mg_{1/3}Nb_{2/3})O_3$-$0.35PbTiO_3$ with an associated lattice mismatch of less than 2%. Although characterized well by transmission electron microscopy these films have yet to be examined for their dielectric properties.

1.2 Objectives of Research

The objectives of this research can be characterized by the following aspects:

- Measure the capacitance of single crystal epitaxial relaxor ferroelectric films of $0.65Pb(Mg_{1/3}Nb_{2/3})O_3$-$0.35PbTiO_3$
- Relate observed dielectric behavior to both atomic structure and microstructure
- Investigate thin films using scanning probe microscopy to provide information related to the piezoelectric response of the films
- Compare properties of single crystal epitaxial films to ceramics and single crystals of similar composition

2 Literature Review of Relaxor Ferroelectrics and their Thin Films

2.1 Ferroelectric Crystals

As shown in Figure 2, of the 32 symmetry point groups 21 are non-centrosymmetric, and 10 of the non-centrosymmetric crystals are pyroelectric, they develop a spontaneous polarization with temperature. The materials have a unique polar axis that exists within the lattice and the total dipole varies with temperature. Ferroelectric materials are a sub-group of the spontaneously polarized pyroelectrics.

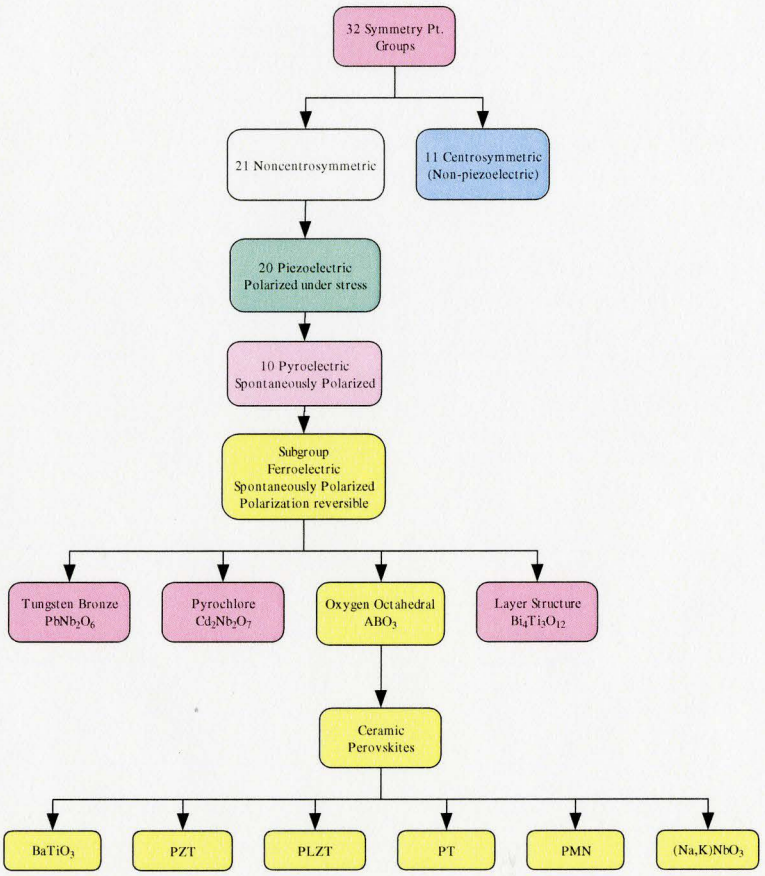

Figure 2: Interrelationship of ferroelectric and subgroups on the basis of symmetry

A crystal is said to be ferroelectric when it has two or more orientational states in the absence of an electric field. It can be shifted from one state to another by the application of an electric field.[1] The orientation states are identical in crystal structure and differ only in the electric polarization vector at null field. The spontaneous polarization only exists in a certain range of temperatures. When the temperature exceeds a certain level, called the Curie temperature (T_c), a phase transition occurs. The Curie temperature is characterized by the disappearance of the spontaneous polarization and a change in the symmetry of the crystal lattice. It also corresponds to the return of normal dielectric behavior of the material.

Ferroelectric materials exhibit some interesting properties which make them uniquely suited to the aforementioned applications. The most oft exploited property being the piezoelectric effect. First discovered in 1880 by Jacques and Pierre Curie the piezoelectric effect is the ability of certain crystalline materials to develop an electric charge proportional to an applied mechanical stress.[6] Conversely, piezoelectric materials also show a mechanical or geometric strain proportional to an applied voltage.

All ferroelectric materials are piezoelectric whereas not all piezoelectric materials are ferroelectric. The piezoelectric effect refers to the ability of a crystal to exhibit electric polarity when subjected to stress due to a small displacement of electric charge within the crystal. The piezoelectric effect is described by two fundamental equations. They relate the elastic variables to the electric variables of the system. The elastic variables, stress (T, N/m^2) and strain (S) are tensor components, while the electric components dielectric displacement (D, $coulomb/m^2$) and electric field (E, V/m) are a

vector quantities. The dielectric displacement refers to the electric flux density per unit area.

$$D = dE + \varepsilon^T E \qquad \text{a)}$$

$$S = s^E T + dE \qquad \text{b)}$$

Equation 1: Equations describing a) direct and b) converse effect in piezoelectrics

The rest of the variables are d a piezoelectric coefficient (coulomb/N), s the material compliance (m^2/N), and ε the dielectric constant. The superscripts indicate that a quantity is held constant[1]. The equations of state for the piezoelectric effect are fundamental in that they exhibit the interplay between the electric and elastic boundary conditions imposed on ferroelectric materials.

2.1.1 Ferroelectric Physics

In order to describe the ferroelectric phenomenon in a general sense a two dimensional hypothetical model of a ferroelectric crystal was developed by Jona and Shirane[7]. The simplified model consists of a crystal with the chemical formula AB existing in a square network as seen in Figure 3

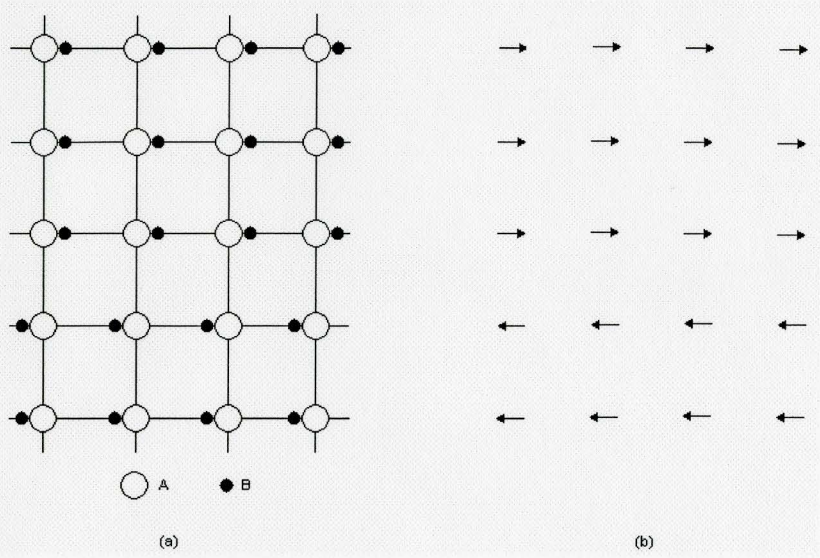

Figure 3: Schematic structure of a fictitious ferroelectric crystal[7]

The A anions and B cations lie in the horizontal plane such that the cations are located at equilibrium closer to one anion than the other. This arrangement is possible if there are two equilibrium positions, as shown in Figure 4, with a minimum value of energy. Thus, in order for the B cation to move from one position to another it must be provided with the energy to overcome ΔE.

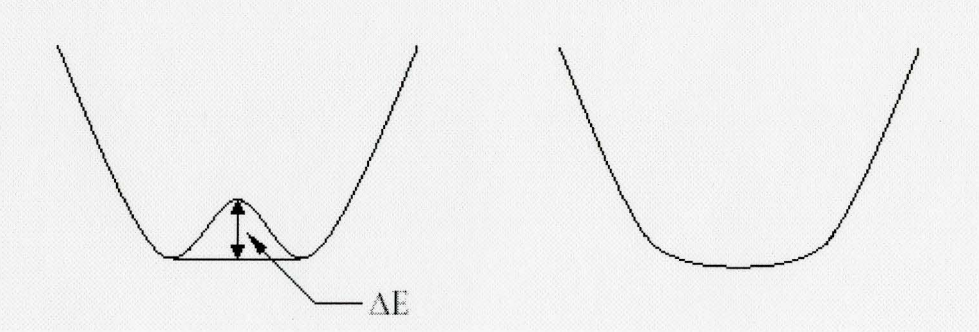

Figure 4: Schematic potential wells[7]

If at a given temperature T all B cations are closer to their A partners on the left, as in the top three rows of Figure 3, every AB group can be visualized as an assembly of

electric dipoles and at that given temperature are spontaneously polarized; the direction of the polarization is the polar axis. The polarization may extend in either direction, as such; the lower portion of Figure 3 would be considered a domain of opposite polarization.

The polarization hysteresis loop is the most recognizable result of the aforementioned example. The hysteresis loop is a graphical representation of the relation between polarization (P), the dipole moment per unit volume, and the applied electric field (E) and is typically measured through the use of a Sawyer Tower circuit. The hysteresis loop and its important features are shown in Figure 5.

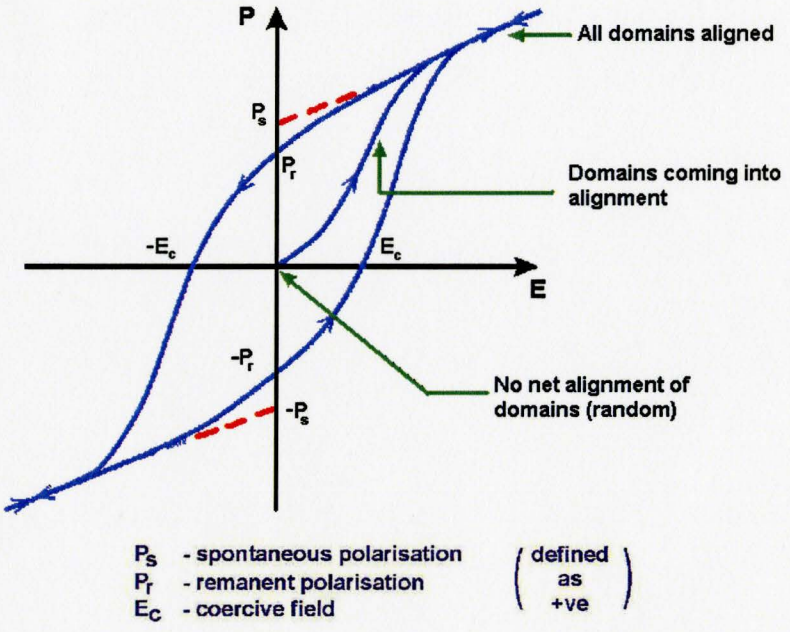

Figure 5: Schematic Ferroelectric Hysteresis Loop

The Sawyer Tower circuit design was first developed in 1930[8] and is used to easily visualize the polarization hysteresis loop on an oscilloscope. The circuit design as first proposed by Sawyer and Tower is reproduced in Figure 6. In this circuit an AC

voltage is used. The voltage across an unknown crystal C_x is put on the horizontal plates of the oscilloscope thus plotting a quantity proportional to the field across the crystal[7]. A linear capacitor C_o is connected in series with C_x and the voltage across C_o is therefore proportional to the polarization of C_x. This voltage is across the vertical plates of the oscilloscope. This construction allows one to not only visualize the hysteresis loop but also to measure the important quantities of spontaneous polarization P_s and the coercive field E_c.

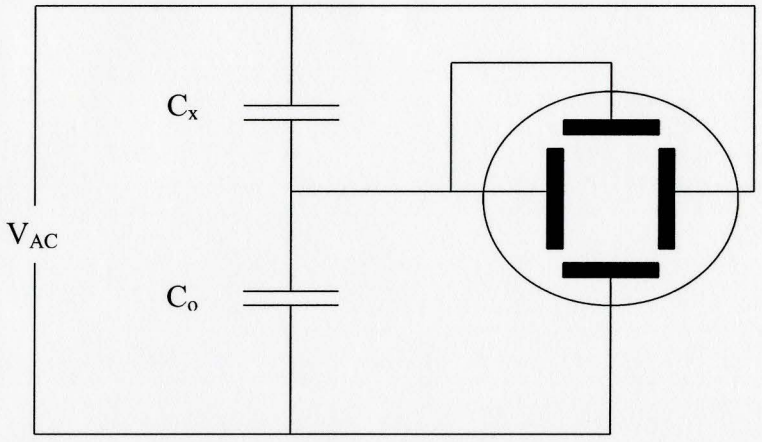

Figure 6: Sawyer Tower Circuit construction[8]

The simplified schematic of the potential wells in Figure 4 demonstrates the fact that the application of a small electric field will cause an increase in energy allowing the cation to overcome the energy barrier ΔE. It is reasonable to then assume that any change in energy, including an increase in thermal energy, may shift the position of the cation. Alternatively, an increase in energy may also change the shape of the potential energy curve leaving only one equilibrium position. When only one equilibrium position exists

the material will behave as a normal dielectric. The temperature at which this occurs is known as the Curie temperature (T_c)

2.1.2 Ferroelectric Domains

A ferroelectric material develops a spontaneous polarization and stress distribution upon cooling from the parent non-polar phase to the ferroelectric phase. In an ideal crystal, the polarization and stress distribution may emerge along several crystallographic orientations with equal probability forming its domain structure. Each region of the uniformly oriented crystal is known as a domain and was shown schematically in Figure 3. The region separating two areas of dissimilar polarization is known as a domain wall, these regions have unique properties which influence the overall behavior of the crystal.

Within a ferroelectric crystal there are two types of domain walls, ferroelectric and ferroelastic. Domain walls that separate different orientations of the spontaneous polarization vector are called ferroelectric domain walls and those which separate different orientations of the spontaneous strain are called ferroelastic domain walls.

Ferroelectric domains are formed in order to minimize the electrostatic energy of depolarizing fields within the crystal. Depolarizing fields are a result of surface charge created at the transition to the ferroelectric state or between two grain boundaries and are oriented opposite to P_s. They arise whenever a non ergodic distribution of spontaneous polarization is formed.[9] Strong depolarization fields are often generated at the grain boundaries and as a result, the single domain state of a ferroelectric ceramic is energetically unfavorable. This energy is minimized by the splitting of the ferroelectric

into domains of opposite orientation. Depolarization fields may also be neutralized by conduction of free charges within the crystal, or free charges associated with surrounding material.

Early studies by Fousek and Janovek[10] established a set of criteria in which one may predict possible stable ferroelectric domain wall orientations between two polarization directions within a perfect single crystal that are outlined below.

- The crystal distorts during the phase transition to the ferroelectric state. The displacement is predicted by the magnitude and direction of spontaneous polarization as well as the piezoelectric and electrostrictive coefficients in the paraelectric phase.
- The possible ferroelectric domain walls for the crystal are defined by crystallographic planes which match exactly following the distortion. This satisfies the condition of electric neutrality at the domain wall.
- The normal component of the spontaneous polarization should be continuous through the domain wall. Otherwise, instability due to electrostatic energy will eliminate it.

The initial theory by Fousek and Janovek works well for bulk crystals, however, stress and strain within thin films required that alternative stability formulations be investigated. Thin film perovskites, particularly those that undergo a cubic to tetragonal phase transition, have a well defined domain structure that has been investigated by Alpay and Roytburd[11] resulting in a domain stability map. Tetragonal perovskites may only have spontaneous polarization that can be oriented along the mutually perpendicular principle axes. Thus, for perovskites there are two types of domain walls which may be present. They separate domains with oppositely oriented polarization (180° domain

walls) and domains with mutually perpendicular polarization (90° domain walls). The 90° domain walls are both ferroelectric and ferroelastic domain walls as they separate different orientations of both spontaneous polarization and strain.

The domain stability map calls for three possible domain structures in a single domain system and an additional three for a polydomain system as shown in Figure 7a. It is shown in Figure 7b that as the misfit strain becomes more compressive that the polydomain structures are favored. The favored domain stability will depend on the substrate orientation. In Figure 7b the substrate orientation is c-oriented (3 in Figure 7a) and the initial structures which are favored consist partially of c-oriented domains. The domain stability is entirely dependent on the misfit strain between the film and substrate and the tetragonality of the crystal. The misfit strain may be manipulated by substrate selection and thermal expansion differences within the heterostructure.

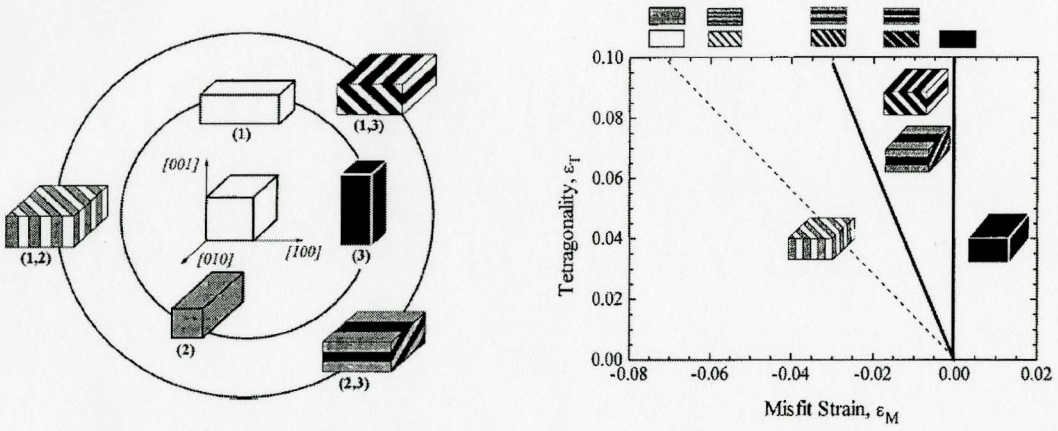

a) b)

Figure 7: Domain stability in thin films undergoing a cubic to tetragonal phase transition a) single and polydomain orientations b) Domain stability map[11]

The domain structure of a ferroelectric material is the primary contributor to its behavior. The structure along with domain nucleation and mobility determine the ferroelectric properties of the crystal which are imposed by the mechanical and electrical boundary conditions as well as the materials history.

2.1.3 Relaxor Ferroelectrics

Lead based relaxor materials were first documented by Smolenskii in the late 1950s.[4] Relaxors are complex perovskites with the general formula of $A(B'B'')O_3$[12] and are characterized by three families of property peculiarities. Firstly, as was mentioned in the introduction, relaxor ferroelectrics have a diffuse, frequency-dependant permittivity maximum with a relaxation spectrum. Therefore, the phase transition does not occur directly at the Curie temperature but instead occurs over a temperature range, hence the

term, "diffuse phase transition." An additional consequence of the diffuse phase transition is that the permittivity maximum can no longer be linked to a single temperature, as such the permittivity maximum for relaxors is commonly referred to as T_m. Secondly, hysteretic response slowly degenerates into a non linear response as temperature increases. This behavior, as shown in Figure 8, signifies that the spontaneous polarization is not lost at the Curie temperature but instead decays more gradually to zero.

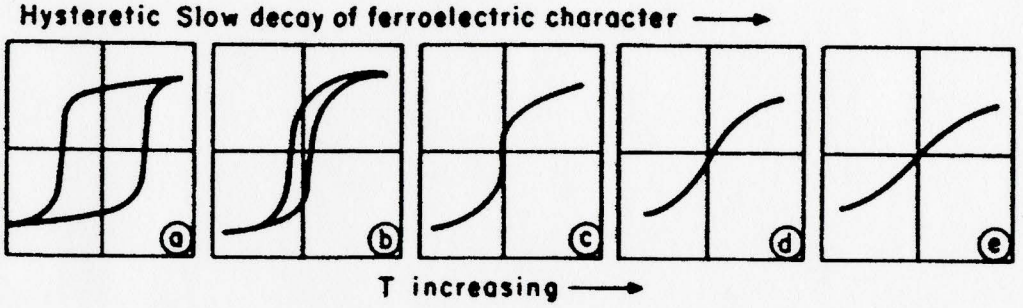

Figure 8: Hysteretic response of relaxor ferroelectric with increasing temperature[5]

Thirdly, optical and x-ray evidence demonstrate that there is no optical anisotropy or x-ray line splitting which would indicate a macroscopic phase change below the Curie temperature (T_c).

2.1.4 Lead Magnesium Niobate-Lead Titanate

The single crystal form of the relaxor ferroelectric $(1-x)Pb(Mg_{1/3}Nb_{2/3})O_3$-$(x)PbTiO_3$ (PMN-PT) has been known to exhibit a piezoelectric and electrostrictive effect that is much greater than that of conventional ferroelectric ceramics.[13] The piezoelectric effect in thin film PMN-0.35PT has been reported between 500-1000 pC/N[14]

Electrostriction is a non-linear coupling between the elastic and electrical fields in a material[9]. It is present in all materials regardless of symmetry. The electrostrictive strain x is defined by the formula:

$$x_{ij} = Q_{ijkl} P_k P_l$$

Equation 2: Strain due to electrostriction

where the electrostrictive coefficient Q_{ijkl} is a fourth rank tensor and P_k, P_l are the vectors of induced polarization.

In addition, compositions of PMN-PT have been found to have an extremely high relative permittivity (~20,000) in single crystal form. Its structure and primary polarization direction in the tetragonal phase are shown in Figure 9.

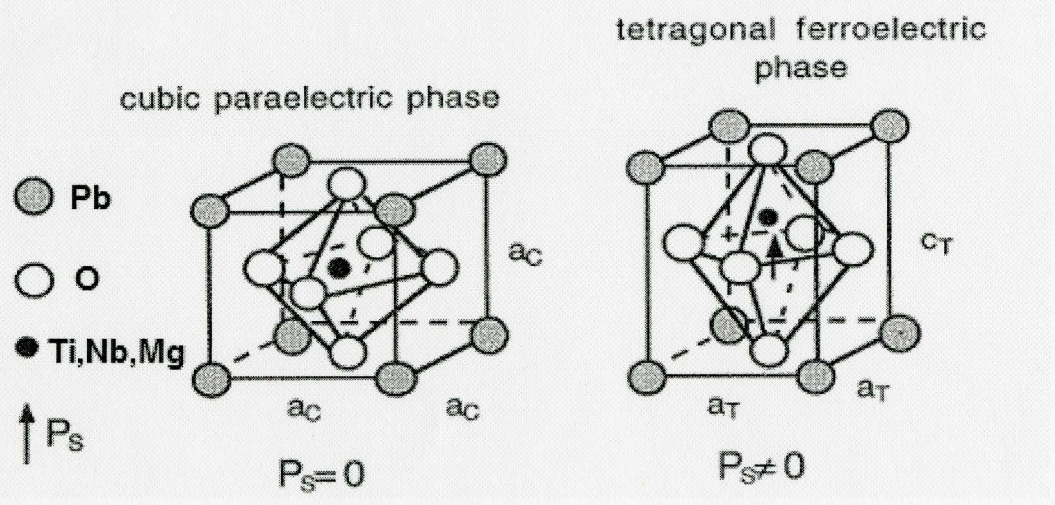

Figure 9: Structure of PMN-PT solid solution in cubic and tetragonal phase[9]

The solid solution of PMN-PT has been extensively studied in the bulk ceramic, single crystal and thin film form as it has interesting properties in the region of its morphotrophic phase boundary (MPB) between x ≈ 30-35%.

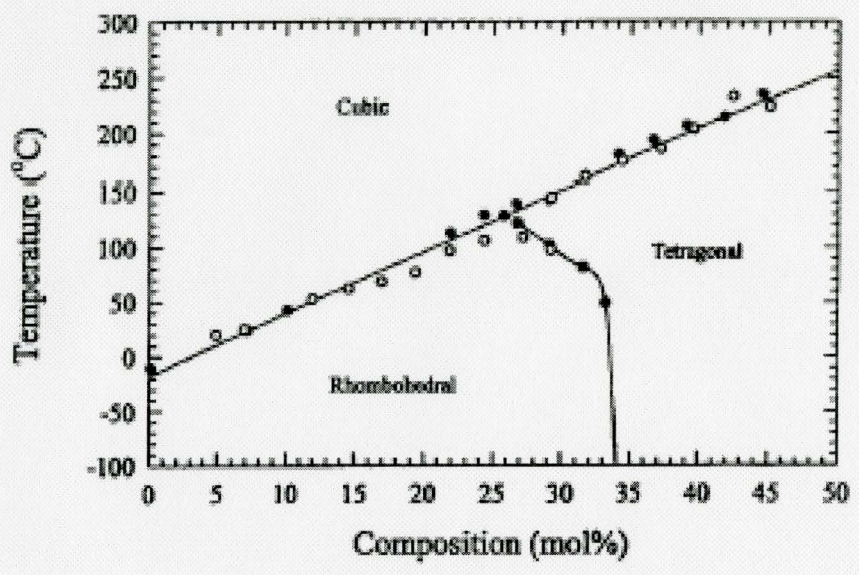

Figure 10: Phase diagram of PMN-PT solid solution[15]

The morphotrophic phase boundary is a nearly temperature independent boundary between two ferroelectric phases where the two structural states differ only in symmetry. It has been found that ferroelectric compositions within the MPB tend to show property extremes within this compositional range[3]. Ceramic compositions within the MPB are also more easily poled as there are effectively more states available to achieve a greater degree of polarization without a corresponding increase in elastic energy.[16]

In general, the single crystal values of the dielectric constant are larger than the bulk ceramic and the bulk ceramic dielectric constant is larger than that of the thin film form. Table 1 lists the characteristics for PMN-0.35PT deposited on various substrates by different deposition methods. The single crystal dielectric constant is included for comparison.

Composition	Deposition Technique/Substrate	Orientation	Relative Dielectric Constant (ε_{33}, 1kHz, T_m)	Dielectric loss factor	Reference
PMN-PT (90/10)	PLD - LSCO/MgO(100)	(001)	2800	0.09	[17]
PMN-PT (70/30)	PLD – LSCO/MgO(100)	(001)	1100	0.06	[17]
PMN-PT (70/30)	PLD – $SrRuO_3/LaAlO_3(001)$	(001)	1700	0.2	[18]
PMN-PT(65/35)	Sol Gel – (111) $Pt/SiO_2/Si(100)$	Random	2900 (10kHz)	0.02	[19]
PMN-PT(65/35)	RF-Sputtering - (001)$SrTiO_3$/La-ST/	(001)	4500		[20]
PMN-PT(65/35)	PLD - LSCO/MgO(100)	(001)	2200	0.05	[17]
PMN-PT(60/30)	PLD - LSCO/MgO(100)	(001)	1200	0.07	[17]
PMN-PT (MPB)	Single Crystal – Modified Bridgeman	(001)	4200 (25°C)		APC

Table 1: Dielectric Characteristics of PMN-PT solid solutions in thin film and single crystal form on various substrates

2.2 Dielectric Theory of Relaxor Ferroelectric

There are various theoretical models that exist which attempt to explain the anomalous dielectric properties of relaxor materials. The Smolenskii model of compositional fluctuation[4], Cross Superparaelectric model,[5] Dipolar glass model[21], and random field[22] theory all lend insight into aspects of the relaxor phenomena. Despite the numerous theories that exist there is not one unified model which can explain all the unique properties however, it is widely accepted that localized ordering plays an important role. The origin of localized ordering and how it controls the dielectric properties of relaxors as a function of temperature is still a matter of debate.

The most popular, and oft cited, model explaining relaxor dielectric behavior was proposed by Smolenskii[4]. As seen in Figure 11 the model theorizes that across any crystal there is a fluctuation in the B-site cation composition causing disorder in the sample. In the case of PMN there is a fluctuation in the ratio of Mg:Nb concentration across the crystal. As a result there are areas of disorder within the crystal causing corresponding fluctuations in the Curie temperature. Therefore, over a wide temperature range there is a mixture of ferroelectric (Polar) and paraelectric (Non-polar) regions with increasing polarization as temperature is decreased. The dielectric response of relaxors was interpreted as a switching of the local spontaneous polarization, P_s within these regions. Thus at a given temperature, T, only the regions with a local T_c equal to T would contribute to the macroscopic dielectric response.

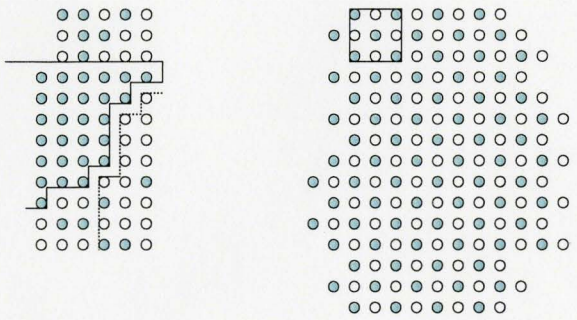

$A(B'B'')O_3$

Disordered phase
B' rich regions
B" rich regions
Relaxor behaviour

Ordered Phase
Uniform composition
Translational symmetry

Sharp transitions

Figure 11: Two-dimensional illustration of order-disorder in hypothetical Smolenskii model

The Cross superparaelectric model[5] similarly suggests that relaxors consist of small non-interacting polar regions each with a local polarization. However, Cross postulated that the potential barrier for reorientation is dependant primarily on the volume of the polar region given that ferroelectricity is a cooperative process. The model suggests that for regions with a size ~100Å the potential barrier required to reorient the local polarization vector would be comparable to the thermal energy of the crystal. Thus, local polarization can vary under thermal agitation and all polar regions contribute to the orientational polarization. Given these conclusions the temperature and frequency dependence of dielectric permittivity is due to the slowing down of local polarization fluctuations.

The dipolar glass model of Viehland et al[21] attempted to fit the electric field dependence of the polarization across a wide temperature range from below T_m to well above the transition to the paraelectric phase. It was postulated based on a direct

comparison of relaxor ferroelectrics with magnetic spin glasses. The primary difference between this model and that of Smolenskii or Cross is that the small polar regions interacted instead of being entirely independent. In addition, it was believed that the local polarization fluctuations occurred above a static freezing temperature denoted T_f.

2.3 Pulsed Laser Deposition

Pulsed Laser Deposition (PLD) is a thin film deposition technique first developed by Smith and Turner[23] in 1965, shortly after the development of the first ruby laser. PLD is performed with in a vacuum chamber where a target, rotating holder and a substrate attached to a heater are located as shown in Figure 12

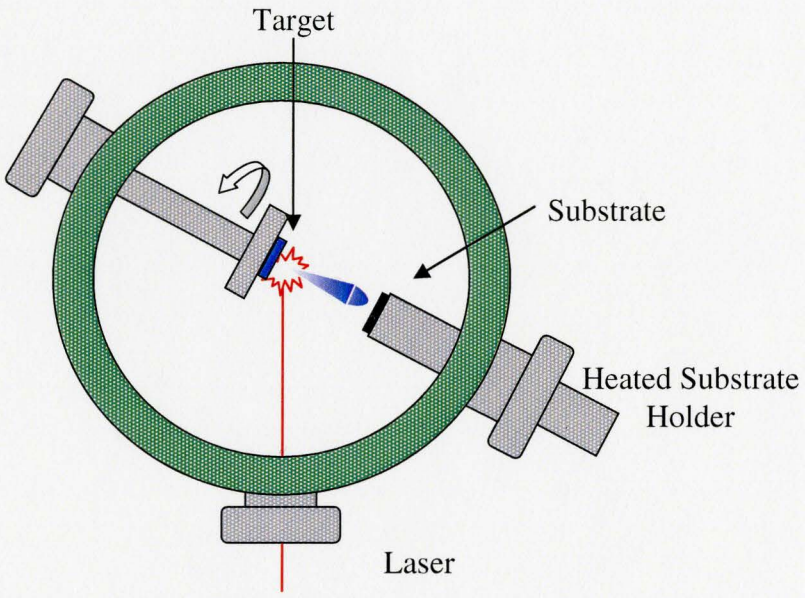

Figure 12: Schematic of pulsed laser deposition chamber

An external high energy laser is focused through a window inside the chamber. The beam strikes the surface of the target and is converted into electronic, thermal, chemical and mechanical energy which in turn ablates the target. A plume of material is ejected normal to the surface of the target composed of atoms, molecules, electrons, ions, clusters and microsized solid particulate. Geometrical arrangement of the laser window, target and substrate ensure that most of the atomic species within the plume are deposited on the substrate soon after ablation.

The technique offers the advantage of flexible, stoichiometric deposition and congruent evaporation. The drawbacks of the method including; micron sized particulates and small deposition angle, limiting the potential for large area scale up. Despite these drawbacks, PLD is capable of growing high quality epitaxial films. Compositional control and film quality are determined through a semi-empirical iterative process involving the optimization of deposition conditions. The deposition conditions are influenced by all elements of the experimental apparatus including the laser, target, substrate, atmosphere and temperature control.

It is well known that deposition with volatile components, such as Pb, have been found to be highly dependent on gas composition, substrate temperature and target composition[24]. The crystallinity of the films is most affected by the substrate temperature increasing with elevated temperature. This is only effective to a certain point as increased vaporization of the volatile constituents may also occur resulting in non-stoichiometric deposition and often the appearance of unwanted phases. The incorporation of volatile

elements with reasonable crystallinity may often only be possible by controlling the background gas pressure and avoid re-evaporation once deposited.

2.4 Thin Film Effects in Ferroelectric Materials

The use of thin film ferroelectrics and their characterization has increased as modern applications necessitate a reduction in size. The reduction in size of ferroelectric films has shown a corresponding reduction in the important properties associated with ferroelectric materials namely coercive field, dielectric constant and spontaneous polarization.[25,26,27,28]

The scaling of the coercive field with film thickness has been studied both theoretically and experimentally ultimately resulting in an empirical relation between the thickness of the film and its associated coercive field. In the size range of 200 nm to 100 μm the coercive field has been found to scale according to the following equation

$$E_c \sim d^{-2/3}$$

Equation 3: Scaling of E_c with thickness[28]

Where d is the film thickness and the exponential term of -2/3 is a product of the nucleation rate per unit area of ferroelectric domains. The determination of the exponent has been proven experimentally and thermodynamically theorized to be solely dependent on the nucleation of new domains excluding the lateral growth of existing domains.

The large relative permittivity of ferroelectrics is the most oft exploited feature of these materials, although, it is well known that thin films have inferior dielectric properties when compared to both ceramics and single crystals. The influence of strain

on the properties of ferroelectric thin films has been treated thoroughly by Pertsev et al[25,29], Maria et al[30], and Wasa et al[31]. Pertsev has published and co-authored numerous articles related to the thermodynamic influence of biaxial strain on the dielectric properties of ferroelectric films. Ultimately, it has been found that epitaxial films often exhibit two dimensional clamping by the substrate material. The associated clamping can result in changes of ferroelectric behavior including additional phase generation or inhibition. The thermodynamic argument supporting these results is directly linked to the misfit strain between the substrate and thin film, which is exacerbated by differences in film and substrate thermal expansion. This is perhaps most well represented by the calculated phase diagram of (001) single domain $BaTiO_3$ as shown in Figure 12. Pertsev et al included the experimentally observed monoclinic *r-phase* and also completed the evaluation by calculating the dielectric constant associated with each phase at room temperature as shown in Figure 13 b).

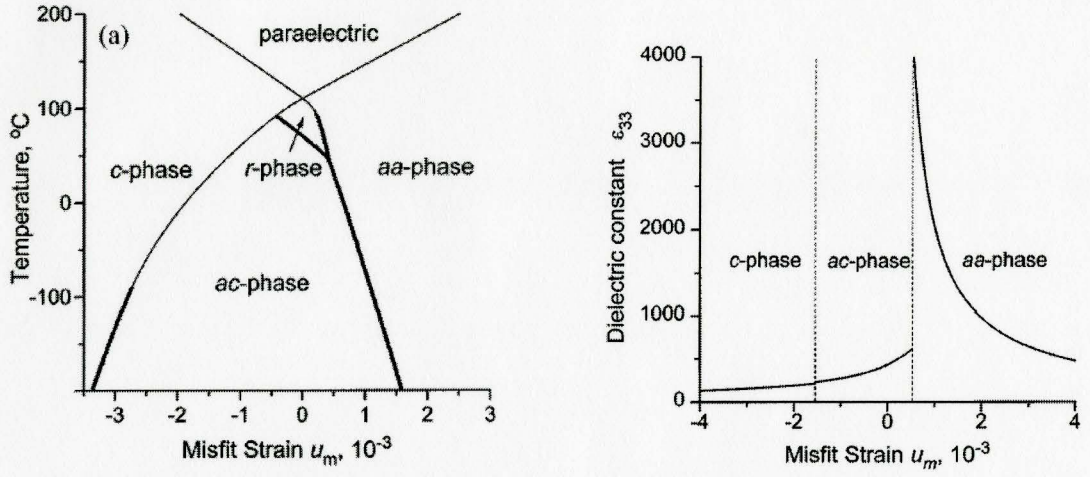

a) b)

Figure 13: Calculated phase diagram vs. misfit strain and associated dielectric constant versus misfit strain for (001) oriented epitaxial $BaTiO_3$[25].

2.5 Dielectric Characterization

The electrical characterization of ferroelectric materials is most important when considering the practical application of the materials. It is also very difficult depending on the geometry and design of the heterostructure. The conventional method of dielectric evaluation is to use a flat plate capacitor structure whereby both the dielectric constant and, in the case of ferroelectric materials, the polarization behavior, via the Sawyer-Tower circuit construction, can be observed. Microstructural limitations dictate the quality of the film that may be deposited on typical electrodes. Thus, alternative characterization methods such as interdigital capacitors may be used.

2.5.1 Interdigital Capacitors

The term interdigital refers to a digit-like periodic pattern of parallel in plane electrodes as shown in Figure 14. An interdigital capacitor operates based on the build up of capacitance between the electrodes associated with the electric field that penetrates into the material sample or sensitive coating. Historically, the interdigital structure has been used to increase the effective length and thus capacitance between electrodes. The first example of an interdigital layout was created by N. Tesla in 1891 where he patented his electrical condenser[32]. This first example consisted of rectangular plates immersed in an insulating fluid. Although development of different capacitor designs continued throughout the 20th century it wasn't until approximately 25 yrs ago when the technology of microdielectrometry emerged. Its emergence initiated extensive use of interdigital capacitors for various sensing applications including, humidity and moisture, electrical insulation, monitoring of curing processes, chemical sensing and bio sensing.[33]

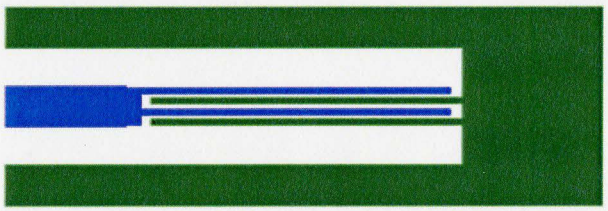

Figure 14: Top view of interdigital circuit design

The principle for operation of an interdigital capacitor is the same as a more conventional flat plate capacitor. A voltage is applied to the electrodes and the impedance across them is measured. However, the primary advantage of this geometry is that access to only one side of the material under test is required.

The transformation of the electric field from parallel plate geometry to an interdigital geometry is outlined in Figure 15. The diagram highlights an important point. The electric field lines pass through the material under test in all three cases and thus the capacitance and conductance between the electrodes depends on the dielectric property of the material as well as material and electrode geometry.

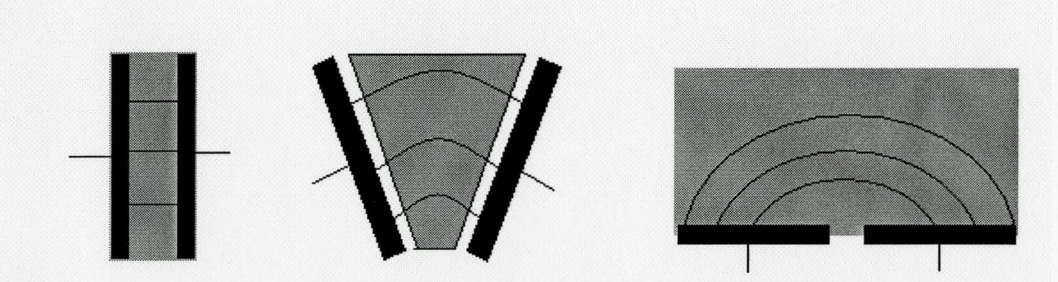

Figure 15: Schematic depicting the bending of electric field lines from a flat plate to an IDC capacitor

The use of interdigital dielectrometry to determine the dielectric constant as opposed to measuring changes in capacitance of a material has had limited use. However, modern electronics demand greater microstructural control which in turn is limiting the available substrates one may use, thus encouraging the use of interdigital capacitors as characterization tools. Improvements in capacitance modeling techniques have enabled researchers to develop new electrode geometries for materials characterization. As such, interdigital dielectrometry for characterization of materials has increased over time.

2.6 Capacitance Modeling

The evaluation and characterization of thin film dielectrics present challenges which are not encountered when evaluating single crystals and ceramics. While single crystals and ceramics are typically evaluated by parallel plate capacitors which adhere to Equation 4, geometrical and microstructural limitations require alternative avenues, such as interdigital electrodes, to be explored for thin films.

$$C = \frac{\varepsilon \varepsilon_o A}{d}$$

Equation 4: Calculation of capacitance in a flat plate construction

In Equation 4, where ε is the dielectric constant of the material ε_o, is the permittivity of free space, A is the area of the top electrode and d is the separation between the plates, the evaluation of the materials dielectric constant is quite simple. The geometry of interdigital electrodes necessitates that alternative formulae should be explored.

The modeling of interdigital electrodes has been explored using both numerical[34,35] and closed form conformal mapping (CM) methods[36,37,38]. Numerical methods were initially explored by Farnell and co-workers by finite difference modeling in the early 1970's[34] Using this model they developed a semi-empirical equation which evaluates the capacitance per unit length of the interdigital finger related to the electrode geometry in terms of the width (w) and period of the electrode (L) and thickness of the film (h), where the period of the electrode refers to the horizontal distance between the

electrode centers. The term K is a geometrical term that was fitted to the quadratic equation and is solely dependent on the electrode width and period.

$$C = K\left\{1 + \varepsilon_s + (\varepsilon_f - \varepsilon_s)\left(1 - \exp\left(-4.6\frac{h}{L}\right)\right)\right\}$$

$$K = 6.50\left(\frac{w}{L}\right)^2 + 1.08\left(\frac{w}{L}\right) + 2.37$$

Equation 5: Numerical model for capacitance as developed by Farnell and co-workers[34]

However according to Farnell, the above equation was believed to only be applicable to films of thickness greater than 1μm and where the permittivity of the film and substrate did not differ by more than 50. It was not until 2001 when Prume and co-workers[35] further evaluated Farnell's model and found it to be applicable to thinner films, on the order of 0.5-0.6 μm with dielectric constants not in excess of ~1000. Although, it was found that as films became thinner the error in the calculation greatly increased.

Closed form analytical expressions for the capacitance of interdigital electrodes were derived by conformal mapping techniques. The derivation, initially explored by Wei[36] utilized complete elliptical integrals of the first kind to map the geometry of a parallel plate capacitor to coplanar electrodes as was shown in Figure 15. The model proposed by Wei was applicable only to a semi-infinite thick film so as not to incorporate the capacitance associated with the substrate. The utilization of partial capacitance methods[37] has extended the CM models to include substrate capacitance.

The capacitance per unit length for interdigital electrodes, as derived by Gevorgian,[37] utilized the partial capacitance method and conformal mapping. Although extensive the model is summarized by Equation 6.

$$C = \frac{\varepsilon_{eq}\varepsilon_o K(k')}{K(k)}$$

Equation 6: Capacitance per unit length using Gevorgian CM

It is easily seen that the equation is analogous to parallel plate geometry where *K(k')* and *K(k)* are complete elliptical integrals of the first kind, the modulii of the integrals are geometrical factors related to the area probed by coplanar electrodes. In addition, ε_{eq} takes into account the capacitance of the thin film as well as the substrate and top layer (superstrate), as the electric field generated between the two electrodes passes both above and below the electrodes.

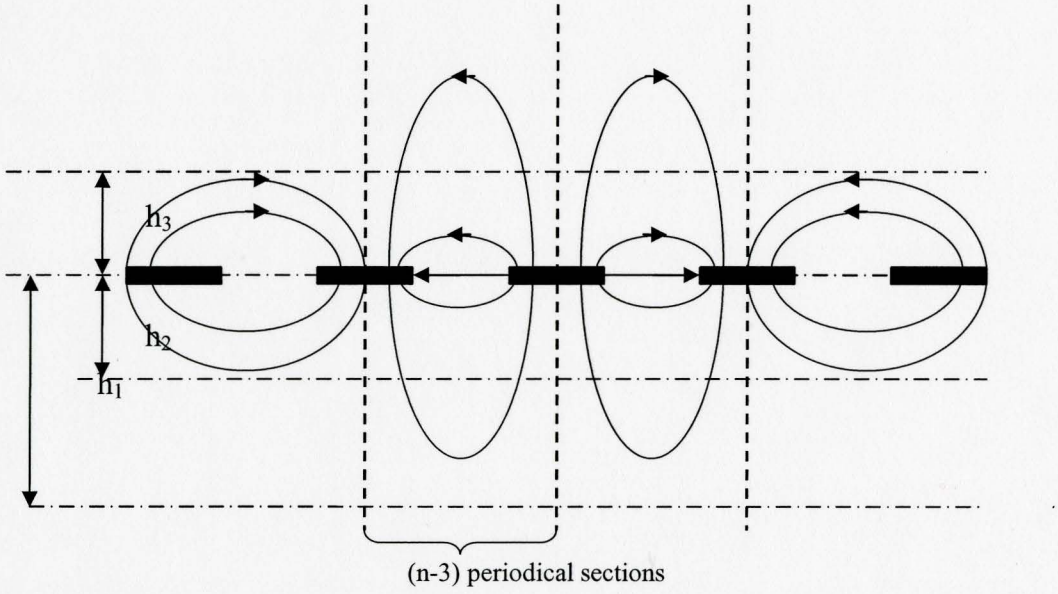

Figure 16: Electric field lines between electrodes in a multilayer capacitor construction (Gevorgian)

The illustration in Figure 16 is used to visualize the electric field lines that exist between the electrodes in an interdigital capacitor. The reference to (*n-3*) periodical sections reflects the use of symmetry within the model in order to simplify the calculations as the capacitance may be multiplied by the number of periodical sections. This model has been interrogated by Igereja[38] and found to be quite suitable for thin films, although the limitations for applicability are not well discussed.

2.7 Piezoresponse Force Microscopy (PFM)

Scanning Probe microscopy has been used to image ferroelectric domains and examine ferroelectric properties with great success over the last 15 years. Its use offers the advantages of being able to image and manipulate ferroelectric domains to the nanometer scales as well as measure certain ferroelectric properties without difficult sample preparation.

Piezoresponse Force Microscopy was preceded by Electrostatic Force Microscopy (EFM) as the first technique implemented to image ferroelectric domains. First published by Saurenbach and Terris in 1990, EFM was accomplished by mounting a cantilever tip on a piezoelectric bimorph and oscillating it with a small AC voltage at a frequency just above the resonant frequency ω_1 of the lever[39]. The lever motion was detected by an optical fiber based interferometer and with the aid of a lock in amplifier. EFM measures the static charge on the surface of the material, thus enabling the observation of different ferroelectric polarization directions in the crystal.[39,40] Although beneficial in ferroelectric observation EFM has several deficiencies as a result of the relatively small signal such as

static charge on the surface, drag due to adsorbed water etc. These hindrances were overcome with the introduction and first use Piezoresponse Force Microscopy (PFM).

The first use of PFM was by H. Birk et al[41] to measure the piezoelectric coefficient in a ferroelectric copolymer of vinylidene fluoride and trifluorethylene. The film was sandwiched between an aluminum layer and a 20nm thick gold electrode. Using an AC voltage piezoelectric surface oscillations were induced and detected with the lock-in amplifier.

It was not until 1994 that PFM was used to study ferroelectric ceramic thin films of lead zirconate titanate.[42] This was quickly followed by the recording of local piezoelectric hysteresis loops within PZT films by Hidaka et al.[43] As interest in the area of PFM expanded systematic studies of domain switching, retention and fatigue were carried out by Gruverman et al [44,45] and validation of the technique using the well known materials of barium titanate, triglycine sulfate, and potassium trihydrogen phosphate single crystals were performed[46,47,48].

2.7.1 Principle of operation

The converse piezoelectric effect is utilized in PFM in order to image domains in ferroelectric films. As discussed in Section 2.1 the application of an electric field will change the dimensions of a piezoelectric material. The fact that the piezoelectric effect can be interpreted as the electrostriction phenomenon biased by the spontaneous polarization leads to the conclusion that the piezoelectric coefficient and spontaneous polarization are directly related.[9]

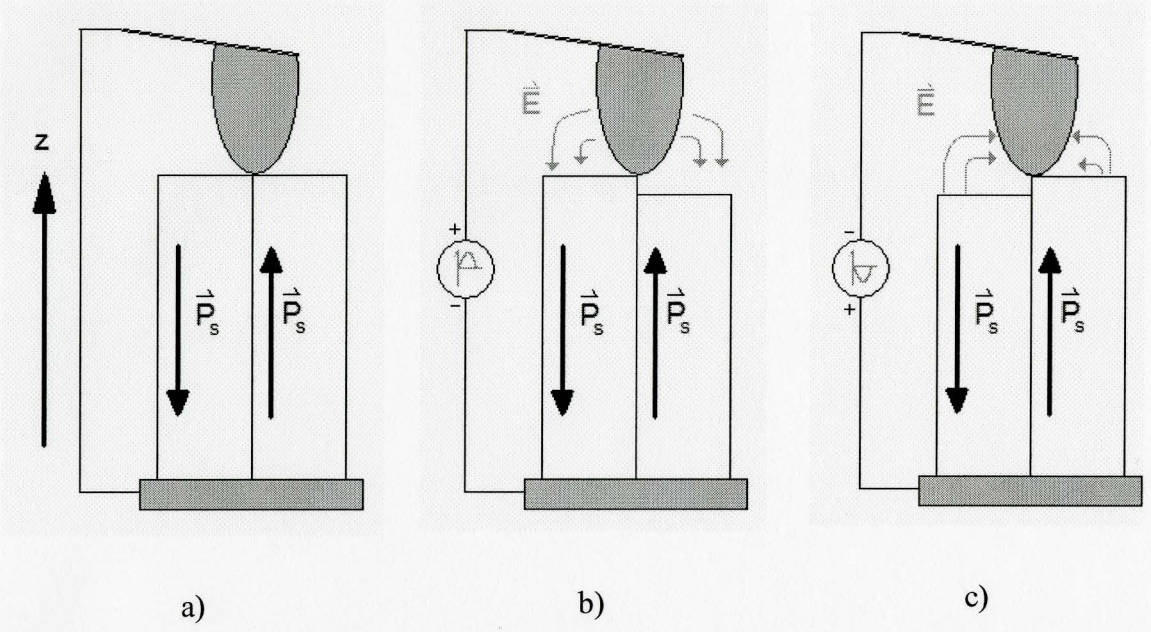

Figure 17: Principle of PFM a) zero bias and no contrast b) positive bias applied to tip change in thickness c) opposite thickness changes with negative bias applied to tip

Piezoresponse force microscopy utilizes the probe tip as a top electrode which may be moved over the sample surface. The imaging mechanism is shown in a simplified manner in Figure 17 with the ferroelectric material between the bottom electrode and conductive tip. The ferroelectric sample consists of two ferroelectric domains with opposite spontaneous polarization perpendicular to the sample surface. When no voltage is applied (Figure 17a) the two domains have the same dimensions in the z-direction. When a voltage is applied between the tip and bottom electrode the electric field generated causes the domains with corresponding polarization to extend and those with opposite polarization to contract (Figure 17b). The opposite is true when the electric field is reversed.

In order to explain the displacement of the sample surface due to the electric field a number of assumptions must be considered.

- The bottom surface of the sample is fixed and the resultant surface displacement is equivalent to the entire piezoelectric displacement. Consideration of displacement at the bottom electrode would reduce the surface displacement[49]
- The electric field is uniform between the probe tip and bottom electrode
- The positive z-axis is oriented from the bottom electrode to the probe tip
- The direction of spontaneous polarization is normal to the film

Using the above assumptions, Equation 1b may be reduced to:

$$\Delta S_z = -d^* E$$

Equation 7: Ideal strain induced by PFM

Where d^* equals d_{33} for positive domains, $P_z > 0$ and $-d_{33}$ for negative domains, $P_z < 0$. The electric field is chosen so as not to exceed the coercive field of the material and reverse the polarization of the material[50]. The deflection of the cantilever in PFM is on the order of 0.2 nm depending on both the piezoelectric coefficient and applied voltage (assuming 4 V and d_{33}=50 pm/V). This length is approaching the lower limit of resolution in the SPM and such a displacement may be obscured by topographic features. Thus, in order to improve the signal to noise ratio the periodic modulation is superimposed on the static deflection of the cantilever and monitored with a lock-in amplifier. The simultaneous monitoring of topographic data with piezoelectric information allows for the comparison of the images. Therefore by replacing E in Equation 7 with $V=V_{AC}\sin(\omega t)$:

$$\Delta S_z = -d^* V_{AC} \sin(\omega t) \qquad \text{a)}$$

or

$$\Delta S_z = \Delta S_o \sin(\omega t + \Phi) \qquad \text{b)}$$

Equation 8: Strain using AC source

Where in Equation 8b, $\Delta S_o = d_{33} V_{AC}$ and Φ is the phase, for positive domains $\Phi = \pi$ and for negative domains $\Phi = 0$. Therefore, opposite orientations of polarization along the z-axis cause the sample to deflect out of phase under a small AC voltage. This is referred to as "voltage modulated SPM" as the ferroelectric domains of different local polarization modify the AC oscillation with their mechanical response.

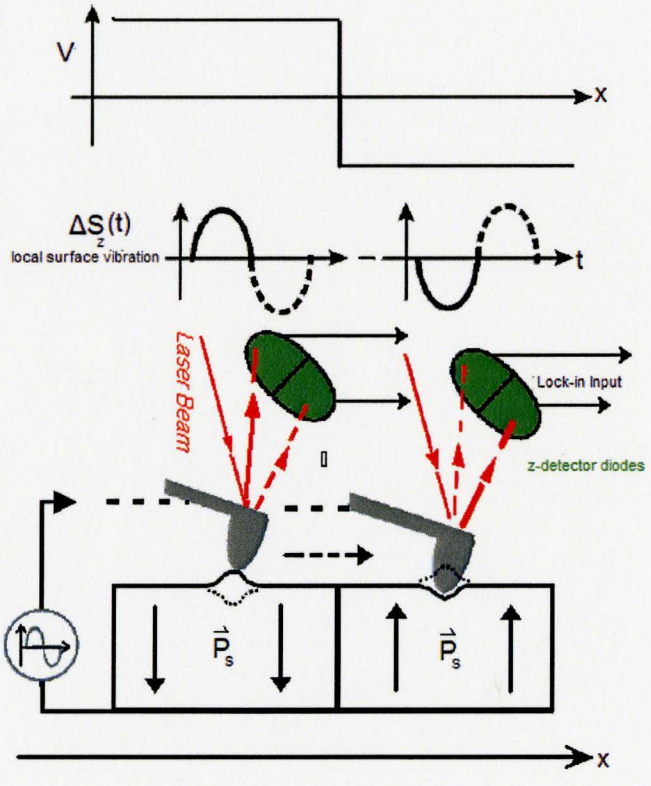

Figure 18: Demodulation of polarization state information from the piezoresponse signal

The detection of the surface displacement is performed using a lock-in technique. Traditionally, the deflection of the SPM tip is monitored using a laser which is reflected by the cantilever on which the tip is mounted. The cantilever deflection due to the surface is converted to an electrical signal using an optical detector and processed in the SPM controller. In PFM the deflection signal also contains the induced surface oscillation due to the applied AC voltage. These oscillations are extracted from the global deflection signal using a lock in amplifier. The lock-in amplifier eliminates any other harmonic components of the deflection signal and thus allows the piezoresponse signal to be separated from the topographic signal. The piezoresponse signal (v_ω) is directly related to the amplitude and phase of the surface vibration by the detector sensitivity (δ):

$$v_\omega = \delta \Delta S_o \cos(\Phi)$$

Equation 9: The piezoresponse signal

The piezoresponse signal thus contains information on the polarization direction via the phase as well as the magnitude of the piezoelectric coefficient assuming that the phase shift is one of the two aforementioned values.

Piezoresponse force microscopy may also measure the in plane polarization vector of a sample based on the shear deformation of the sample surface parallel to itself. The detection of shear in the ferroelectric is based on friction which induces a lateral motion of the SPM tip. The lateral motion of the tip is transferred to the cantilever as torsion and detected using the SPM controller's ability to measure cantilever torsion. The

formulation of the piezoresponse signal is much the same as in detection of perpendicular domains however using different components of the piezoelectric coefficient.

3 Experimental Techniques

3.1 Thin Film Deposition

Thin film deposition of 0.65PMN-0.35PT was performed with a KrF laser, operating at 6 Hz and 248nm with laser power equal to 300mJ/pulse. The oxygen pressure was 400 mTorr and the substrate temperature was 650°C, a process which was developed by Maria et al.[18] but optimized for the composition of PMN-35PT[51]. The time of deposition was varied between 6-45 minutes depending on the thickness required. To ensure perovskite phase pure samples in the thin film XRD analysis was completed using the *Bruker D8 Advance Diffractometer* with a CuKα source.

The deposition of the $BaTi_{0.5}Nb_{0.5}O_3$ electrode layer was completed in a similar manner as the dielectric layer. It was also performed with a KrF laser, operating at 10 Hz and 248nm with laser power equal to 300mJ/pulse, under vacuum and a substrate temperature of 850°C,

Two heterostructures were prepared during experimentation and drawings are shown in Figure 19, (note that the figures are not to scale). The single layer sample (Figure 19 a) consisted of 200nm of 0.65PMN-0.35PT deposited on 0.5 mm thick (001) oriented $MgAl_2O_4$ substrate. The multilayer heterostructure had 50 nm of 0.65PMN-0.35PT with a 50 nm diffusion barrier layer of $MgAl_2O_4$ followed by 200 nm of $BaTi_{0.5}Nb_{0.5}O_3$ on a 0.5 mm thick (001) oriented $MgAl_2O_4$ substrate. The $BaTi_{0.5}Nb_{0.5}O_3$ layer acted as a conductive oxide electrode. The important properties of the materials

related to the deposition are found in Table 2 and representative heterostructures used in the characterization are found in Table 3

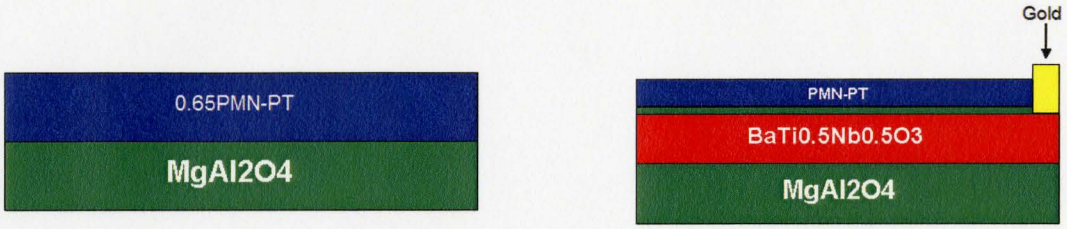

a) b)

Figure 19: Drawing of experimental heterostructures a)single layer sample b)multilayer heterostructure

Parameter	$MgAl_2O_4$	PMN-0.35PT	$BaTi_{0.5}Nb_{0.5}O_3$
Lattice Constant (Å)	8.083	4.024	4.090
Thermal Expansion (ppm/°C)	7.45	~8[18]	unknown
Structure	Cubic	MPB (Tetragonal/Rhombohedral)	Cubic

Table 2: Important characteristics of materials used in sample heterostructures

Sample id #	Structure (Top -> Bottom)	Characterization
PMNT 07	PMN-PT/ (001)$MgAl_2O_4$	Dielectric
PMNT 08	PMN-PT/ (001)$MgAl_2O_4$	TEM
PMNT 18	PMN-PT/ $MgAl_2O_4$ /$BaTi_{0.5}Nb_{0.5}O_3$/(001)$MgAl_2O_4$	SPM/TEM
PMNT 50	PMN-PT/ $MgAl_2O_4$ /$BaTi_{0.5}Nb_{0.5}O_3$/(001)$MgAl_2O_4$	SPM
PMNT 40	PMN-PT/ (001)$MgAl_2O_4$	Dielectric
PMNT 45	PMN-PT/ (001)$MgAl_2O_4$	Dielectric
PMNT 56	PMN-PT/ $MgAl_2O_4$ /$BaTi_{0.5}Nb_{0.5}O_3$/(111)$MgAl_2O_4$	SPM

Table 3: Representative heterostructures and characterization performed

3.2 *Lift off Photolithography*

The interdigital and flat plate capacitors were prepared by traditional liftoff photolithography techniques on the surface of the single layer heterostructures, a single crystal and ceramic sample. Like all cleanroom techniques, cleanliness of all equipment is essential for effective deposition. As such, all materials and glassware was cleaned thoroughly using deionized water and dried with nitrogen prior to use.

The sample was mounted in the centre of the ½" spin head and pressed down to ensure a good seal with the O-Ring. There is a vacuum suction through the spin head, which holds the sample in place on the spinner chuck. A filtered syringe was filled with positive photoresist. The air bubbles were carefully removed from the tip and one drop of

photoresist was then placed in the centre of the sample. The sample was spun at 5000rpm for 30 seconds.

The sample was then removed from the chuck and carefully placed in a covered Petri dish and allowed to dry for 5 minutes. After drying the sample was soft baked on a hotplate preheated to 90°C for approximately 60 seconds.

The sample and chrome on glass mask were mounted in the mask aligner. The sample was oriented in a direction convenient for aligning with the mask, this is important when working with asymmetrical samples as one must ensure that the whole device structure is placed on the sample. The sample was then brought in contact with the mask surface using the Z-position micrometer. If the sample was found to not be aligned properly with the mask the sample was again separated from the mask and adjusted using XY micrometer adjustments or stage rotation. Once aligned the sample was brought in contact with the mask and pressed against the surface until an interference pattern was seen on the edge beads of the sample. The sample was exposed with an energy of 45mJ calculated by multiplying the lamp power, as shown on the lamp power source, by the exposure time, exposure times varied between 5 and 6 seconds. It is important that one does not watch this process as the UV lamp source has a high intensity and may cause damage to the eyes.

Immediately following exposure the samples were rinsed under deionized water and placed in a Petri dish filled with Toluene for 5 minutes, this step is required in order to roughen the surface of the photoresist and aid in lift off after metallization. The samples were then allowed to air dry and developed using *351 Microposit Developer.*

A graduated cylinder was used to measure one part of *351 Microposit Developer* and five parts of deionized water. The solution was then mixed in a 500mL beaker. The sample was placed vertically in the developer using plastic tweezers and the beaker was agitated for 30 seconds. The sample was then removed from the developer and the process was stopped by rinsing the sample under deionized water.

Metallization was performed in an UHV deposition system located in the clean room. The main chamber has a 15 kW multi-hearth e-beam evaporation source. A multilayer deposition of 250 Å titanium followed by 1250 Å of platinum was completed. The titanium layer was used to promote adhesion of the electrode as it is known that platinum does not adhere well when in direct contact with PMN-PT[52]

Metallization was followed by the final lift off procedure whereby the sample was placed in a 500mL beaker partially filled with Acetone. The sample was agitated and allowed to soak until the devices were clearly visible. When all the unwanted metal was removed the sample was removed from the acetone and rinsed with acetone then methanol and finally by deionized water.

3.3 Transmission Electron Microscope Sample Preparation

Cross-sectional transmission electron microscope samples were prepared for both single layer and multilayer samples of (001) oriented 0.65PMN-0.35PT deposited by PLD. This method of sample preparation was used in order to make the film-substrate interface parallel to the electron beam.

Cross-sectional samples were prepared by cleaving two thin slides (approximately 1 mm wide) normal to the interface of the thin film and substrate. The slides were then glued together, face to face, using epoxy. Silicon bars were added to both substrate sides to create a sandwich structure. The thickness of the epoxy must be carefully controlled in order to promote good adhesion while preventing delamination of the heterostructure. Following the preparation of the structure, conventional TEM sample preparation including polishing, dimpling and ion milling was completed.

The microstructural characterization by TEM was performed on both the single layer and multilayer heterostructures. The characterization was performed on a *JEOL 2010F Field emission TEM/STEM.*

3.4 Electronic Characterization Techniques

The capacitance measurements were conducted on single layer, ceramic and single crystal samples of PMN-PT with a *HP4194A Impedance Gain/Phase analyzer* as a function of temperature (273 – 473 K) and frequency (1kHz – 100kHz) with a RMS excitation voltage of 1 V calibrated in both open and short circuit capacitance measurements. They were performed on films of 200 nm thickness. The thickness of the sample is dependent on the PLD deposition time and was measured using the TEM. The dielectric measurements were made using a *GGB industries Picoprobe Model 40A (GSG)* probe set. An open measurement was taken immediately after each measurement to compensate for capacitance differentials between fingers due to thermal expansion. The experiments were completed using an iterative approach so as to cover all of the required

parameters for the samples. The experimental design for the capacitance measurements is found in Figure 20.

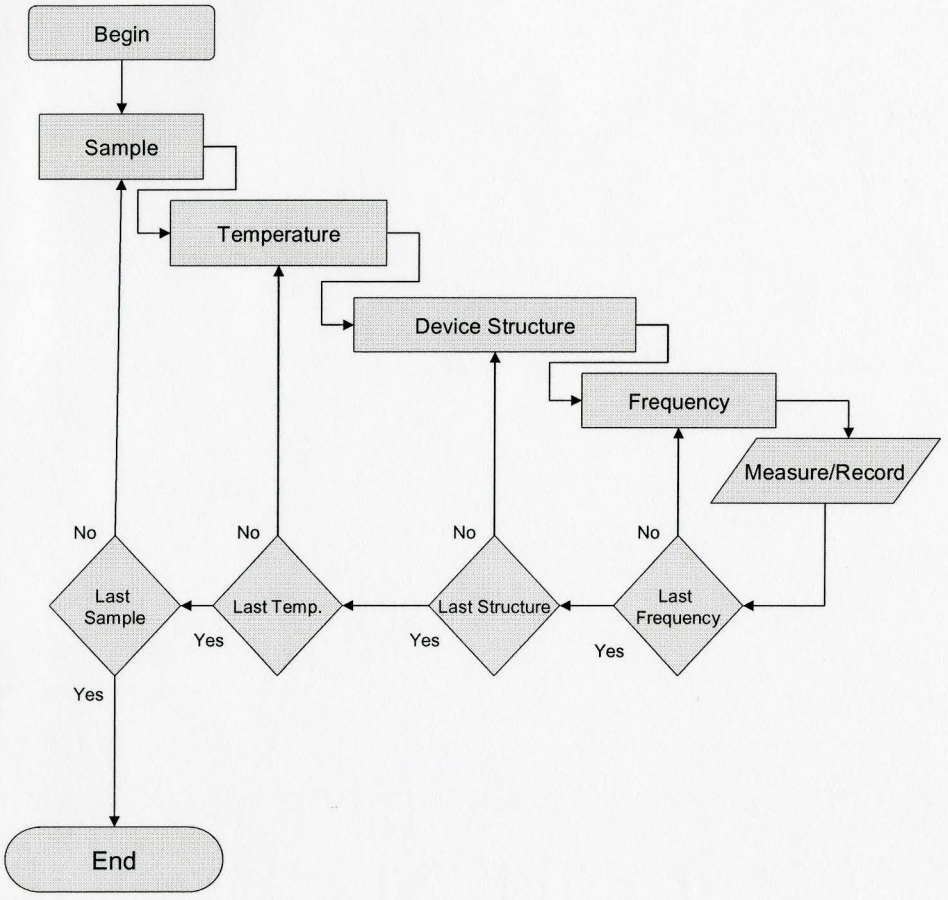

Figure 20: Flowchart depicting experimental design and execution

3.4.1 Electric Field Modeling

As discussed in chapter two several authors have developed analytical methods for the modeling of capacitance.[37,34] The Gevorgian model was used and has been extended, using the dielectric constant of the substrate and single crystal as a free variable for the extraction of the dielectric constant. The Gevorgian model was used to ensure that the results obtained with Finite element modeling were reasonable.

The model calculates capacitances based on symmetrical periodical sections for finger geometries where the number of fingers n, is greater than or equal to 4. In our design n=4 fingers. In this case there is a capacitance calculated for an equivalent periodical section (C_4) in addition to the capacitance due to a three finger electrode denoted as (C_3) in the model. The total capacitance per unit length is equal to the sum of these two numbers. The capacitance for C_n and C_3 are calculated by Equation 10:

$$C_n = (n-3)\varepsilon_o \varepsilon_{en} \frac{K(k_o)}{K(k_o')} l \qquad \text{a)}$$

$$C_3 = 4\varepsilon_o \varepsilon_{e3} \frac{K(k_{o3})}{K(k_{o3}')} l \qquad \text{b)}$$

Equation 10: Capacitances calculation for a) (n-3) periodical sections and b) capacitance of three finger IDC

Where $K(k_o)$ *and* $K(k_{o3})$ are the complete elliptical integrals of the first kind with modulii k_o and k_{o3} respectively ε_{en} and ε_{e3} are the equivalent dielectric constant for the partial capacitance for C_4 and C_3 due to cover layer, thin film and substrate. For the substrate only calculation the thin film and substrate dielectric constant were set as equal. The modulii k_o and k_{o3} were calculated as in Equation 11

$$k_o = \frac{s}{s+g} \qquad \text{a)}$$

$$k_{o3} = \frac{s}{s+2g}\sqrt{\frac{1-\left(\frac{(s+2g)}{(s+2s+2g)}\right)^2}{1-\left(\frac{s}{(s+2s+2g)}\right)^2}} \qquad \text{b)}$$

Equation 11: Modulii of elliptical integrals for a) (n-3) periodical section and b) 3 finger section

The inverse modulus $k' = \sqrt{1-k^2}$ where k is either k_o or k_{o3}. The capacitance calculations also account for the equivalent dielectric constants ε_{en} and ε_{e3} due to the partial capacitance of each layer, they were calculated as shown in Equation 12

$$\varepsilon_{en} = 1 + q_{1n}\frac{\varepsilon_1 - 1}{2} + q_{2n}\frac{\varepsilon_2 - \varepsilon_1}{2} + q_{3n}\frac{\varepsilon_3 - 1}{2} \qquad \text{a)}$$

$$\varepsilon_{e3} = 1 + q_{13}\frac{\varepsilon_1 - 1}{2} + q_{23}\frac{\varepsilon_2 - \varepsilon_1}{2} + q_{33}\frac{\varepsilon_3 - 1}{2} \qquad \text{b)}$$

Equation 12: Calculation of the equivalent dielectric constant for the a) (n-3) periodical section and b) 3 finger section

Where ε_1, ε_2 and ε_3 are the dielectric constants of the substrate, thin film and cover-layer respectively and the q values are geometric variables once again utilizing elliptical integrals for the partial capacitance of each layer defined by Equation 13.

$$q_{in} = \frac{K(k_{in})}{K(k_{in}^{'})}\frac{K(k_{o}^{'})}{K(k_{o})} \quad \text{a)}$$

$$q_{in} = \frac{K(k_{i3})}{K(k_{i3}^{'})}\frac{K(k_{o3}^{'})}{K(k_{o3})} \quad \text{b)}$$

Equation 13: Calculation of q values for the a) (n-3) periodical section and b) 3 finger section

The modulii of the elliptical integrals for the q values are:

$$k_{in} = \frac{\sinh\left(\frac{\pi s}{2h_i}\right)}{\sinh\left(\frac{\pi(s+g)}{2h_i}\right)}\sqrt{\frac{\cosh^2\left(\frac{\pi(s+g)}{2h_i}\right)+\sinh^2\left(\frac{\pi(s+g)}{2h_i}\right)}{\cosh^2\left(\frac{\pi s}{2h_i}\right)+\sinh^2\left(\frac{\pi(s+g)}{2h_i}\right)}} \quad \text{a)}$$

$$k_{i3} = \frac{\sinh\left(\frac{\pi s}{2h_i}\right)}{\sinh\left(\frac{\pi(s+2g)}{2h_i}\right)}\sqrt{\frac{1-\sinh^2\left(\frac{\pi(s+2g)}{2h_i}\right)}{1-\sinh^2\left(\frac{\pi s}{2h_i}\right)}} \quad \text{b)}$$

$$k_{03} = \frac{s}{s+2g}\sqrt{\frac{1-\left(\frac{(s+2g)}{(2s+2g}\right)^2}{1-\left(\frac{s}{(3s+2g)}\right)^2}} \quad \text{c)}$$

Equation 14: Calculation of modulii of elliptical integrals for q values for the a) (n-3) periodical section and b) and c) 3 finger section

In Equation 14a and Equation 14b h_i is the thickness of the associated layer where i=1,2,3 h_1, h_2, and h_3 would be the thickness of the substrate, thin film and cover-layer respectively. The values of s and g are the effective width of the electrode and the spacing

between each finger both of which are equal to 10μm in our geometry. The effective width of the electrode is also dependent on the electrode thickness which was calculated for our specific geometry.

The finite element modeling of the electric fields for the extraction of the dielectric constant of the material was performed using *Ansoft Maxwell 2D V10 Electromagnetic Field Finite Element Simulation* software. It is a commercial software package whereby one may define the geometry of the structure to be studied and assign associated variables to each layer. The Finite element mesh is initially defined by the program and then refined iteratively until the desired energy error as set by the user is achieved. The simulator calculates the electric fields arising from potential differences and charge distributions and the capacitance matrix is found by solving the finite element mesh applying a 1 volt excitation to the test conductor and grounding all other signal conductors included in the matrix. At the simplest level the capacitance is defined as the amount of energy stored between two conductors, thus the energy is calculated as:

$$U = \frac{1}{2} CV^2$$

Equation 15: Energy calculation at each node of the Finite Element Mesh

The capacitance is then directly found by manipulating the equation to solve for *C*. Given that the voltage is set to 1 V the capacitance is then equal to 2 times the energy *U*. For further treatment of the solution the reader is referred to the technical notes included with *Ansoft Maxwell 2D*.

For the single layer heterostructure the dielectric constant of air and substrate were set to 1.006 and 9 while the thickness of the film, air layer and substrate were set to 200nm, 5mm and 0.5mm respectively. The dielectric constant of the thin film was varied between 5 and 1000 and plotted versus the output capacitance of the model. These values were then used to interpret the output capacitance of the *HP4194A Impedance Gain/Phase analyzer.*

3.5 Piezoresponse Microscopy

Piezoresponse imaging was completed on the multilayer heterostructures. The experimental apparatus for the piezoresponse microscopy consisted of a scanning probe microscope (SPM) operating in contact mode, a lock in amplifier, and AC voltage source and a DC voltage supply. The SPM was a commercial *Digital Instruments Nanoscope IIIa* using a CSC37/Ti-Pt/50 probe tip provided by *Micromasch.* All experiments were completed under ambient conditions at room temperature.

Contact to the bottom electrode was provided by mounting the samples on a wafer where silver paste provided contact between the SPM and electrode (Figure 21)

Figure 21: Multilayer heterostructure mounted on a wafer with silver paste connection

4 Results and Discussion

4.1 Single Layer Samples

4.1.1 Electric Field and Capacitance Modeling

The dielectric constant of the substrate and substrate/thin film heterostructure were determined by measuring the capacitance in an interdigital capacitor. Given that the dielectric constant of the substrate and top air layer are known the variation in the dielectric constant of the film is the only free variable. It was with this understanding that electric field modeling was used in order to determine the dielectric constant of the thin film. The experimental design was tested by using a bare substrate of $MgAl_2O4$ with a known dielectric constant between 8 and 9 as a standard.

To verify the applicability of *Ansoft Maxwell FEM* software a model of the electric field between interdigital capacitors was created. The electric field lines based on post processing electric field vector calculations agree well with the vectors as shown by Gevorgian[37] and Mamishev et al.[33] The results from the electric field modeling as shown in Figure 22 clearly indicate that the assumption of a null plane, indicated by A' is valid. This assumption is necessary for the calculation of the capacitance according to the various conformal mapping models of Gevorgian[37], Wei[36] and Igereja[38]. The null plane simplifies the calculations for the analytical models as it introduces symmetry within the structure and allows one to use multiples of the finger capacitances to calculate the total capacitance of the IDC as shown in Equation 10a

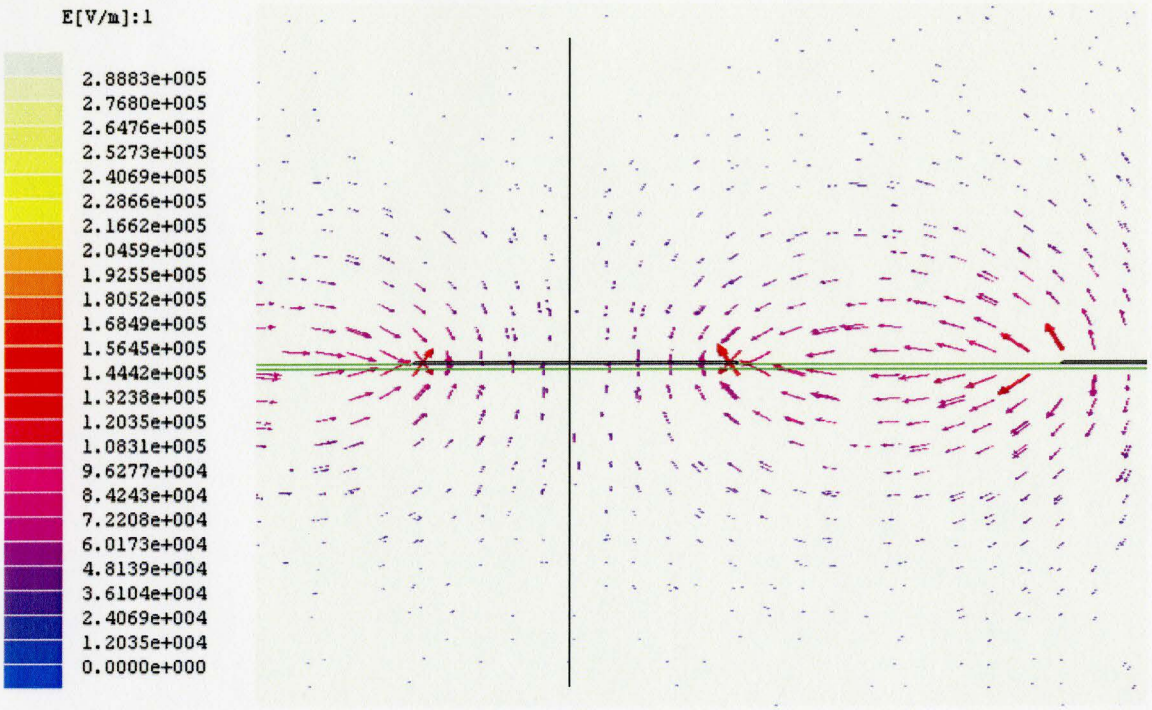

Figure 22: 2D Electric field vectors for IDC structure as calculated by Maxwell

Figure 23 demonstrates the change in capacitance versus dielectric constant as calculated by Maxwell for various thickness of dielectric film with a constant number of fingers, and finger width, spacing and length, 4, 10μm, 10μm and 2480μm respectively. It is seen that in the region of interest, between 150-220 nm that the relationship between capacitance and the dielectric constant for each thickness is linear. Thus, the extraction of the dielectric constant for the material may be easily interpolated from the graph if the thickness of the film is known. It is also known that as the thickness of the film increases its effect on the total capacitance of the heterostructure increases and, as Wang et al[53] previously demonstrated using conformal mapping techniques, the total capacitance

deviates further from linearity as the dielectric constant of the film increases relative to that of the substrate. This effect may be neglected for the samples from this study as the thickness of the film is much thinner that that of the substrate.

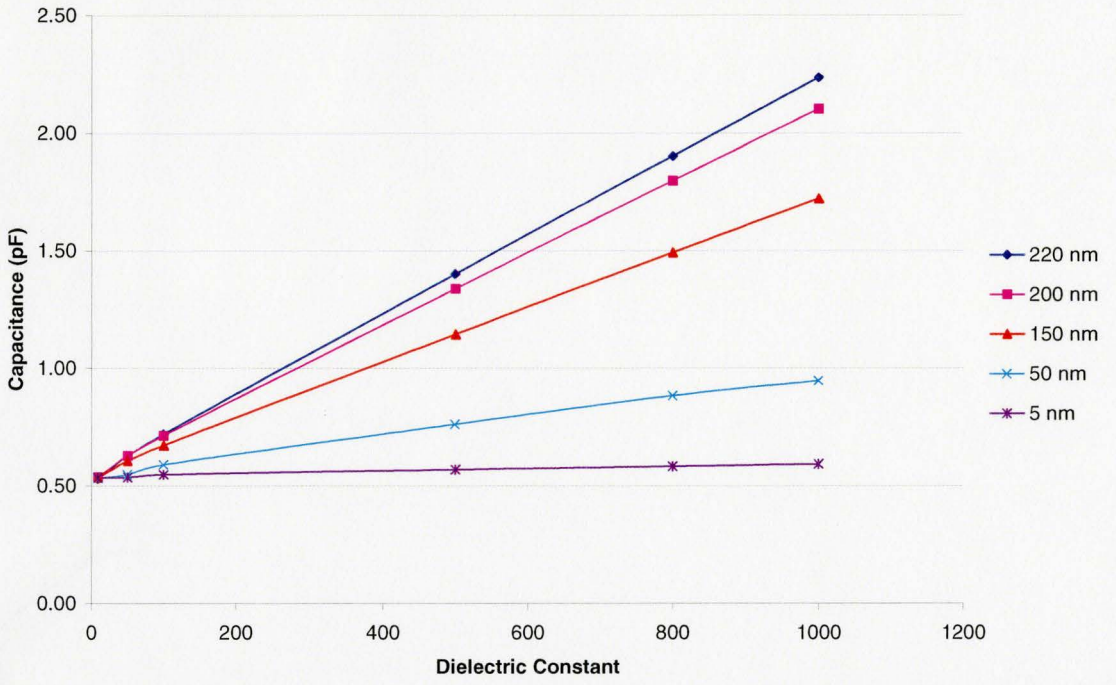

Figure 23 Dielectric constant versus capacitance for various dielectric thicknesses

Investigation and application of the Gevorgian conformal map to our heterostructure shows that its use to determine the capacitance is applicable as long one criteria is met, the effective width of the fingers, *seff*, does not greatly exceed the thickness of the film. This limiting feature was mentioned in the original article by Gevorgian et al[37] with a simplification of the modulii for the elliptical integrals in the case where $seff/h >> 1$. However, even when the simplification was used the modulii of the elliptical integrals $K(k)$ and $K(k')$ approach 0 and 1 respectively. Thus, when the elliptical

integral with modulus k' is calculated it approaches ∞ and the equivalent dielectric constant as shown in the following maple output (Figure 24) cannot be calculated:

(24)-dielectric film

$$> k(24) := \sqrt{2}\, e^{\left(-\frac{P g}{2 h2}\right)}$$

$$k(24) := .8816779558\ 10^{-17}\sqrt{2}$$

$$> k(prime24) := \sqrt{1 - k(24)^2}$$

$$k(prime24) := 1.000000000$$

$$> K(24) := \int_0^{2\pi} \frac{1}{\sqrt{1 - k(24)^2 \sin(\theta)^2}}\, d\theta$$

$$K(24) := 6.283185308$$

$$> K(prime24) := \int_0^{2\pi} \frac{1}{\sqrt{1 - k(prime24)^2 \sin(\theta)^2}}\, d\theta$$

$$K(prime24) := \text{Float}(\infty)$$

Figure 24: Maple output for thin dielectric layer

Given that the elliptical integral approaches infinity the calculation of equivalent dielectric constant as per Equation 12 is undefined. One is unable to compute the capacitance for a multilayer structure for a very thin film unless the fingers are suitably modified.

This difficulty does not arise when measuring the capacitance of the bare substrate and, as a result conformal mapping was only used in order to determine if the results for finite element analysis were consistent with the analytical models.

4.1.2 Dielectric Results

In order to ensure that the capacitance differential measured was due to the thin film and not the substrate, identical interdigital capacitors were deposited on a substrate sample of $MgAl_2O_4$ with a known dielectric constant of 8-9. The capacitance measurements were completed in a frequency range of 0.1 to 100 kHz and a temperature range of 298-423K. The structure was then modeled using both conformal mapping and FEM.

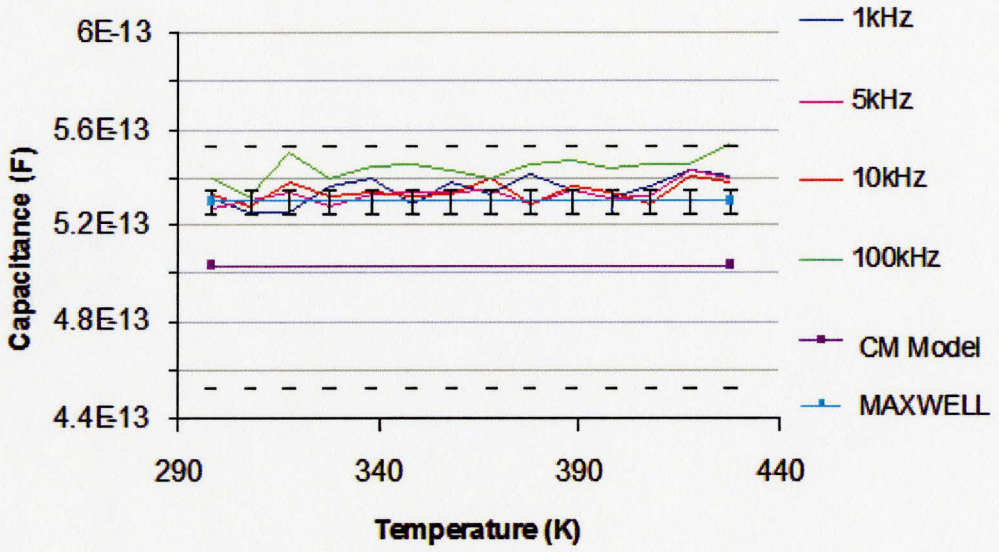

Figure 25: Measured Capacitance of Substrate sample versus temperature

It is seen in Figure 25 that the capacitance values of the substrate as measured do not vary with temperature and there is negligible frequency dispersion. The Gevorgian Conformal Mapping (CM) model matches the data for the substrate when the modeling error is taken into account. A ~10% error in the CM model is expected due to both the RF finger layout and fringing fields at the IDC finger ends which were not taken into account using the 2D model. The Maxwell FEM calculations have an additional level of

accuracy due to the fact that the fringing fields from the RF electrode configuration are taken into account. The FE model matches the experimental values very well when an input dielectric constant for the $MgAl_2O_4$ substrate of 9 is used.

Thus, given the confirmation of the temperature and frequency independence of the $MgAl_2O_4$ over the parameters of interest, one may assume that any changes in the capacitance are due to the thin film PMN-0.35PT. This is shown by the measured capacitance of PMNT45 in Figure 26.

In Figure 27 the frequency and temperature dependence of the capacitance of the thin film is apparent. Additionally, prior to dielectric constant extraction the diffuse nature of dielectric constant is seen. As the temperature approaches 400 K and extends beyond 473 K one may see the broad diffuse dielectric maximum associated with T_m in relaxor materials.

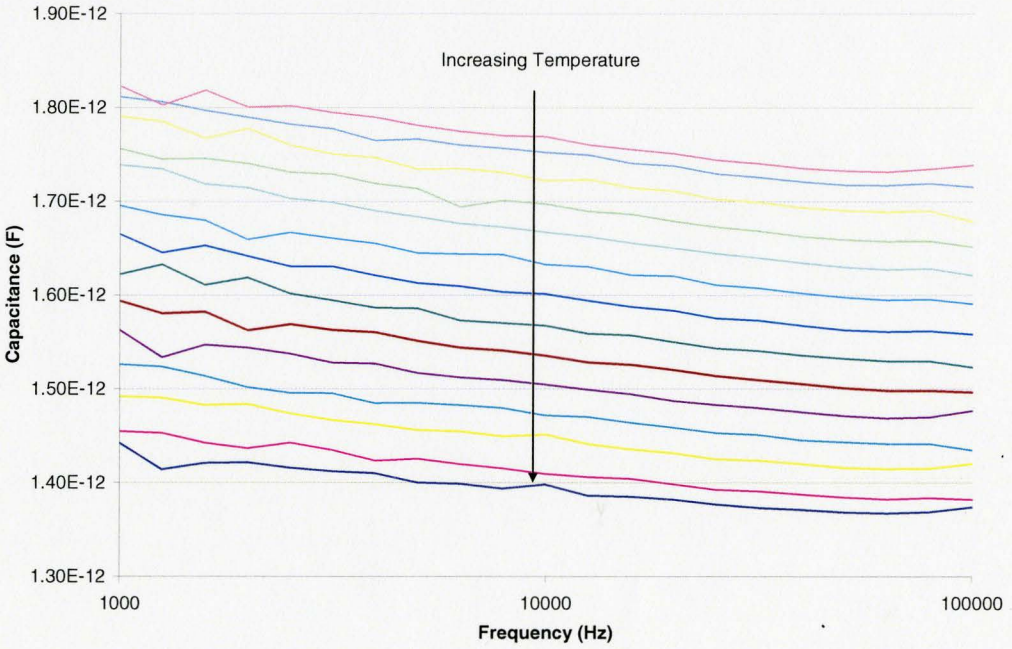

Figure 26: Capacitance versus frequency with increasing temperature from 273 K to 423K

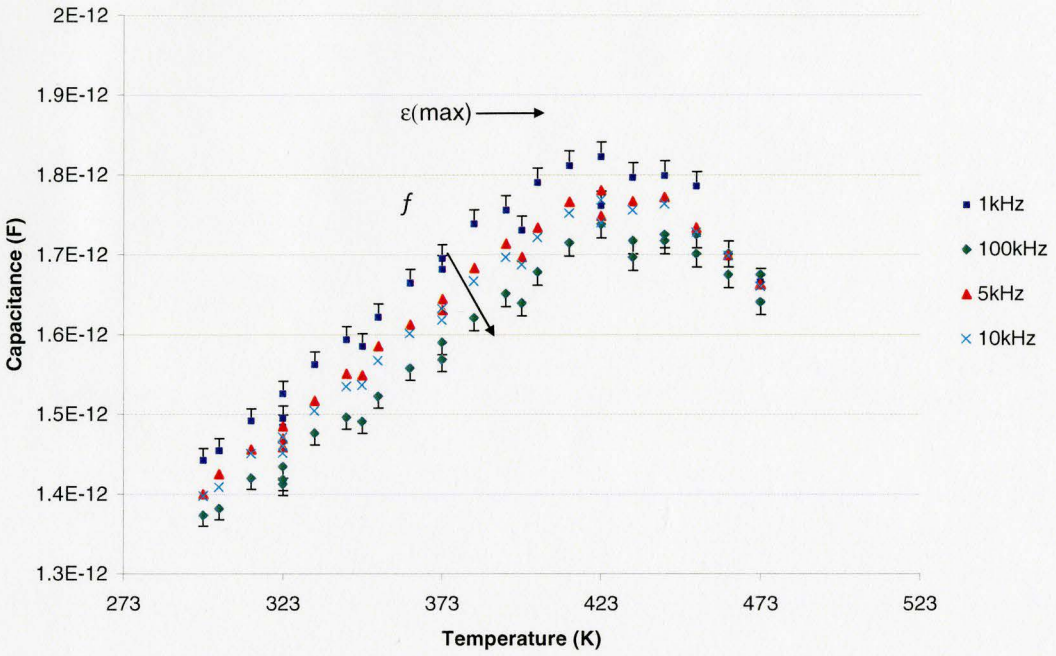

Figure 27: Measured capacitance vs. temperature for frequencies 1kHz-100kHz (PMNT 45)

The solid solution of PMN-PT has been extensively studied in the bulk ceramic, single crystal and thin film form. It is known that the dielectric constant varies depending on both the physical and chemical properties. In general though, the single crystal values of the dielectric constant have been found to be larger than the bulk ceramic and the bulk ceramic dielectric constant is larger than that of the thin film form. The dielectric constant also increases with the amount of PMN in the solution[54]. For thin film PMN-0.35PT oriented in the (100) orientation the reported dielectric constant varies from 2200[55] to 2700,[27] at T_m and 1kHz.

For the films in this study an iterative extraction of the dielectric constant using an isotropic model of the permittivity was considered despite the fact that the dielectric

constant in PMNT is known to be anisotropic. This was completed for single crystal, ceramic and thin film samples. This assumption was considered to be valid as E-field modeling, as seen in Figure 22, shows that at the finger edge the field is essentially orthogonal through the film and should thus be measuring ε_{33}.

The single crystal samples provided by *MTI Ceramics* were supplied with a composition within the rhombohedral side of the MPB and a nominal ε_{33} between 4000-6000 at room temperature and 1kHz, after poling. The ceramic samples provided by *SensorTech* had a known composition of PMN-0.35PT and a nominal ε_{33} of 2700.

As expected the single crystal clearly demonstrates the broad dielectric maximum characteristic of relaxor ferroelectrics (Figure 28). The maximum dielectric permittivity for this material is 18,000 at a T_m of approximately 410 K and 1kHz. The values of the dielectric constant as well as the location of Tm indicate that the composition of the single crystal is between 30 and 35% $PbTiO_3$ when compared with other reported values for PMNT. It is clear that at room temperature the dielectric constant calculated by FEM is slightly lower than that reported by the materials specifications. Although, the measured dielectric constant as provided was obtained immediately after poling of the crystal. It would be expected that over time a reduction in the dielectric constant would occur without the material being poled once again.

The ceramic material (Figure 29) appears to show dielectric response similar to that of a regular ferroelectric. The onset of the peak dielectric constant is rapid and seems to drop off quickly. The dielectric maximum is 5300 at ~463K and 1kHz

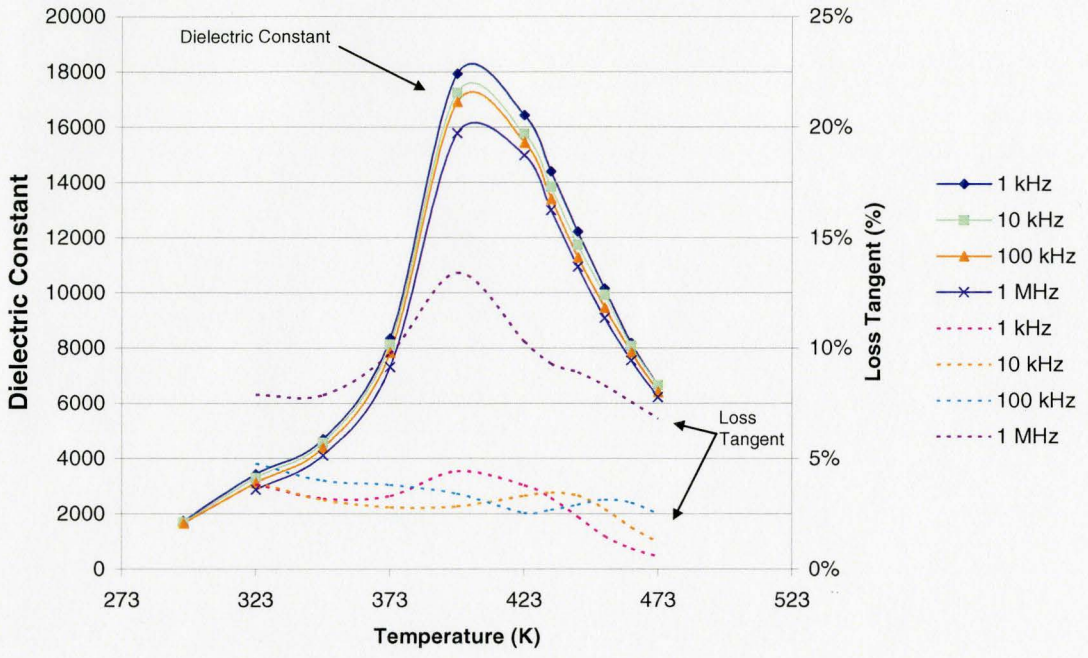

Figure 28: Dielectric constant of single crystal using Maxwell FEM extraction

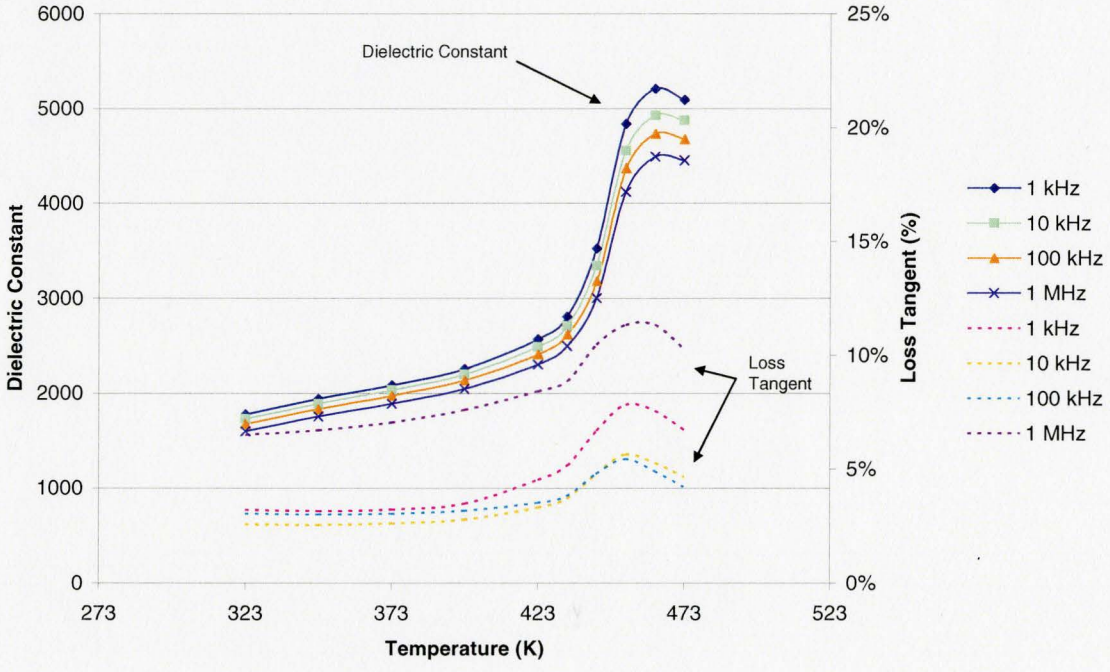

Figure 29: Dielectric constant of PMNT ceramic using Maxwell FEM extraction

The dielectric behavior of the thin film is shown in Figure 30. Using Maxwell FEM the dielectric constant for the thin film from the capacitance data yields values ranging from 561 – 799 at 1kHz and 518 – 746 at 100kHz when the temperature is varied from 273-473K. Additionally, the temperature dependence of the dielectric maximum (T_m) is higher than that seen and predicted in literature which is approximately 410K, [56,57,] These measurements show that T_m appears to be approximately 420K.

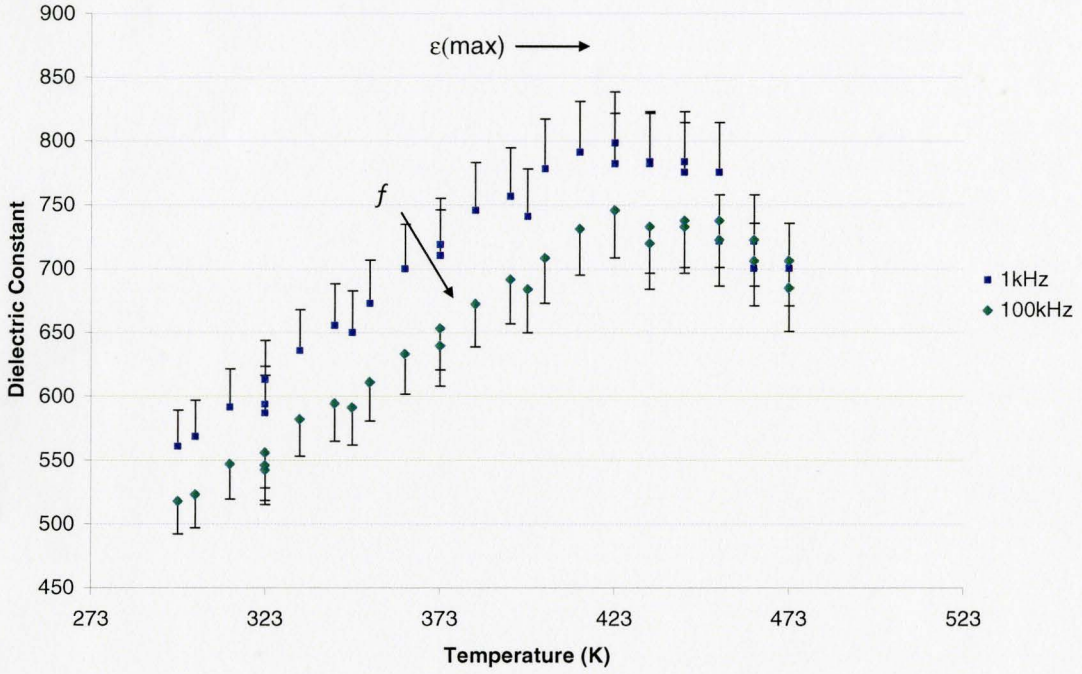

Figure 30: Dielectric constant of the sample PMNT 45 using Maxwell FEM extraction

The values for the thin film are lower than expected when compared with the results of Tantigate[17], Wasa[20] and Kumar[57] and Krupanidhi[58] whom all reported dielectric constants in excess of ~1000 and as high as 2700 at T_m for thin films. The decrease in dielectric constant and shift in T_m could be due to four effects.

Firstly, it has been suggested that substrate clamping may suppress the development of the cubic to tetragonal phase transition in thin film perovskites. This phenomenon should be enhanced by the minimization of the lattice mismatch and by closely matching the thermal expansion coefficient. By doing so one may control the deposited phases as shown in the "misfit strain-temperature" phase diagram[29] Thus, given the epitaxial (001) orientation of the films and tendency for a ferroelastic monodomain state as calculated by Alpay and Roytburd[11] in the as deposited film, it is probable that that substrate clamping has occurred. In addition, due to the misfit strain-temperature phase diagram it is likely that there is a dominance of 180° ferroelastic domains and the formation of 90° domains for strain relief in the tetragonal to cubic transition can not occur. It was speculated by Donnelly et al[56] that strain relief is essential in order to maintain the dielectric maximum as published for single crystal PMN-35PT.

Secondly, regarding the shift in dielectric maximum to higher temperature Pertsev[59] and Maria[26] have suggested that unrelaxed strain in thin film ferroelectrics will shift the permittivity maximum. The Pertsev model suggests that this is due to biaxial stress imposed by the lattice mismatch. This effect would be exacerbated in our samples for two reasons. Firstly, there would be an increase in stress as the PMNT heterostructure was heated due to the difference in thermal expansion coefficients between the PMNT and $MgAl_2O_4$. Secondly, our samples are believed to be single crystal materials based on previous thesis work by Zhuoying Chen. Traditionally, in bulk ceramics and thin films with a poor lattice match, grain boundaries, domain formation, domain rotation and dislocations allow for tension release.

Thirdly, it is well known that the dielectric response of PMNT is dependent on the direction of measurement and the direction of maximum polarization. For tetragonal materials the dielectric constant is often reported in the ε_{33} direction where the applied electric field and long axis, [001] are parallel. The dielectric constant of ε_{33} and ε_{31} can vary by as much as 30%. The specifications of single crystal PMN-PT made by *APC International* indicate, for their composition in the MPB, the dielectric constant for ε_{33} is 6300 while along the ε_{31} it is 4400. Thus, the dielectric constant as extracted by FEM when an isotropic model is used is likely an average of multiple measurement directions.

Finally, the deposition of PMNT films was completed using pulsed laser deposition. The volatility of Pb during deposition may have resulted in a lead deficiency in the thin film samples. The unique dielectric characteristics of relaxor ferroelectrics are believed to be due to localized compositional inhomogeneities of the central atom in the perovskite structure, Mg, Nb, and Ti in the case of PMN-PT. Although there is not any direct evidence of pyrochlore, the lead deficient phase, within the sample small amounts may still be present.

4.1.3 Microstructural Characterization

Although extensive microstructural characterization of thin film PMN-0.35PT films were completed previously by Zhouying Chen,[51] a return to the microstructural characterization was necessary in order to correlate the above results to the microstructure and elucidate the theories as expressed in literature.

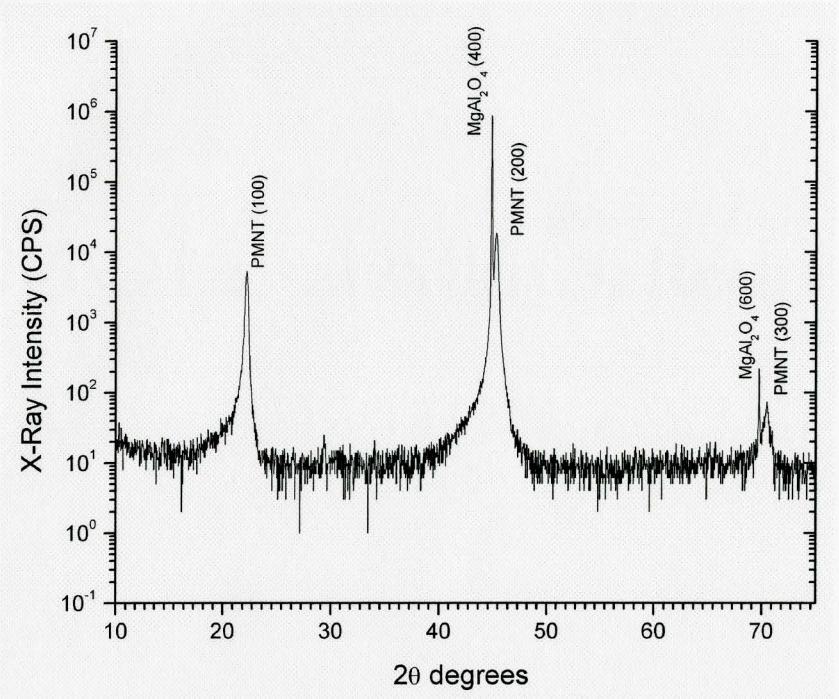

Figure 31: Typical XRD Pattern of PMN-0.35PT on $MgAl_2O_4$ Substrate (PMNT14)

The optimization of the thin film deposition by Zhouying Chen resulted in consistent depositions of well matched thin films and no evidence of pyrochlore in the samples. Figure 31 shows a typical XRD pattern of the PMN-0.35PT on the substrate for samples tested for this work. As expected the (100) reflection of PMNT is located at 2θ of approximately 22° and the (200) reflection is at approximately 44°. The expectation is based on the characteristic reflections from the powder XRD database for cubic PMN where the (100) reflection is located at 2θ= 21.928° and the (200) reflection at 44.715°.

The XRD pattern indicates the presence of only one orientation for the PMNT film. However, given the presumed epitaxial deposition there is little indication as to whether the sample is a single crystal or a well textured polycrystalline material. A cross-sectional structural examination of the material was completed using transmission

electron microscopy (Figure 32). When compared with previous results the film microstructure is consistent. The brightness contrast across the film is very uniform with only slight variations which may be due to low angle misorientations within the film. In addition, there does not appear to be any grain boundaries or other large angle misorientations present within the film.

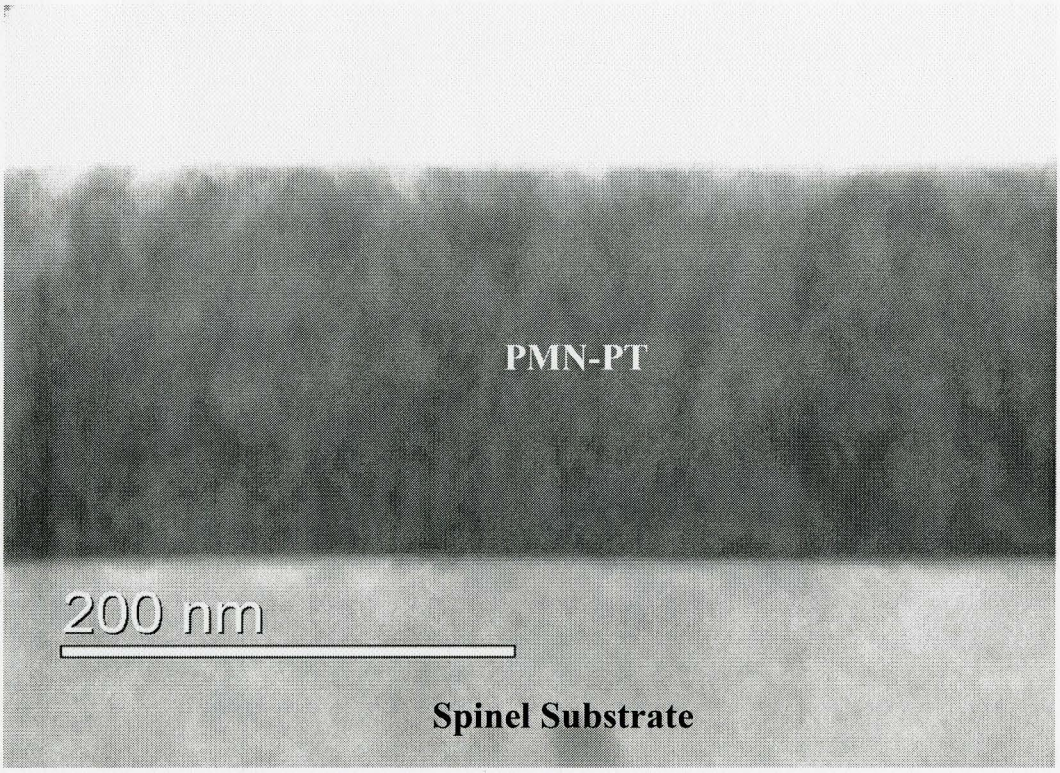

Figure 32: Bright Field TEM image of PMNT on $MgAl_2O_4$ substrate (PMNT27)

To confirm epitaxial deposition, a straight line trace from the substrate to the film on the (100) zone axis (ZA) was completed and convergent beam electron diffraction (CBED) patterns were taken with representative patterns shown in Figure 33. The diffraction patterns show that the film and substrate were deposited epitaxially and there is no evidence of misorientation.

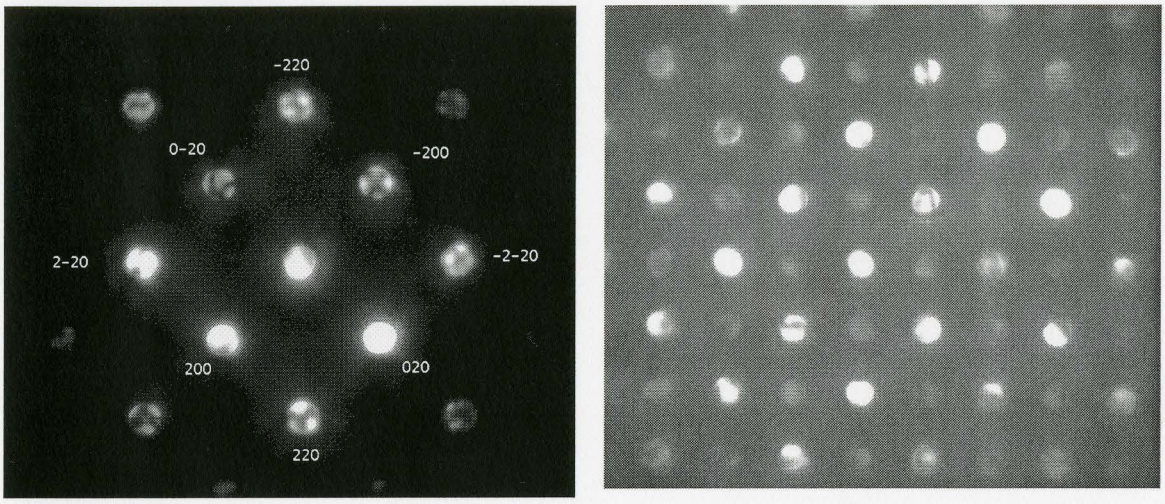

a) Spinel (100) ZA in single layer sample

b) PMN-PT on Spinel (100) ZA in single layer sample

Figure 33: CBED pattern on the (100) ZA of (a) substrate (b) PMNT-0.35PT film

It is clear by examination of the CBED patterns as well as the bright field image and XRD pattern that the thin film is a well oriented epitaxial single crystal. Thus, as postulated in the preceding section, the quality of the heterostructure is likely the primary contributor to the reduction in relative permittivity and the increase in temperature dependence of permittivity.

It is possible that the effect of substrate clamping may be reduced by creating freestanding films, as was done by Maria et al with barium strontium titanate[26]. In addition, induced strain due to thermal expansion at higher temperatures should also be investigated.

4.2 Multilayer Samples

4.2.1 Piezoelectric Response

Piezoelectric response microscopy has been used by numerous authors to characterize thin film ferroelectrics as direction of polarization and effective piezoelectric hysteresis loops can be investigated on a nanometer scale. Shvartsman et al[60,61] as well as other authors have published extensively on the piezoresponse characteristics of PMN and PMN-PT.

Multilayered heterostructures are required to complete piezoresponse microscopy in order generate an electric field through the film. Typical bottom electrodes, $La_{0.5}Sr_{0.5}CoO_3$, Au, and Pt have lattice constants that vary significantly from those of PMN-PT allowing one to create textured (001) oriented films or randomly distributed polycrystalline films. In order to compare the results of the well developed single layer thin films, a conductive oxide bottom electrode of $BaNb_{0.5}Ti_{0.5}O3$ was developed for this study that has a lattice constant of 4.09Å to once again match well with the lattice constant of PMN-PT (4.024Å) and $MgAl_2O_4$ (8.083Å) in order to deposit single crystal thin films. This was completed in both the (001) and (111) orientation.

Immediately apparent in the topographic AFM image (Figure 34) is the granular structure of in both the (001) and (111) oriented samples. This is markedly different than in the single layer heterostructure. The average grain size is approximately 200 nm in both samples. The RMS roughness Figure 34 a) and Figure 34 c), are 5.50 nm and 8.71 nm respectively. There is apparently a difference in the shape of the grain with a more

faceted structure shown in the Figure 34 c). However this is an artifact in the image due to the fact that these images were taken in contact mode AFM and the difference in cantilever stiffness between the two images has 'smeared' the edges of the grains. Thus, a determination of the exact grain structure from these images would be speculatory. Further investigation of these structures was therefore completed with TEM and is examined in the section 4.2.2.

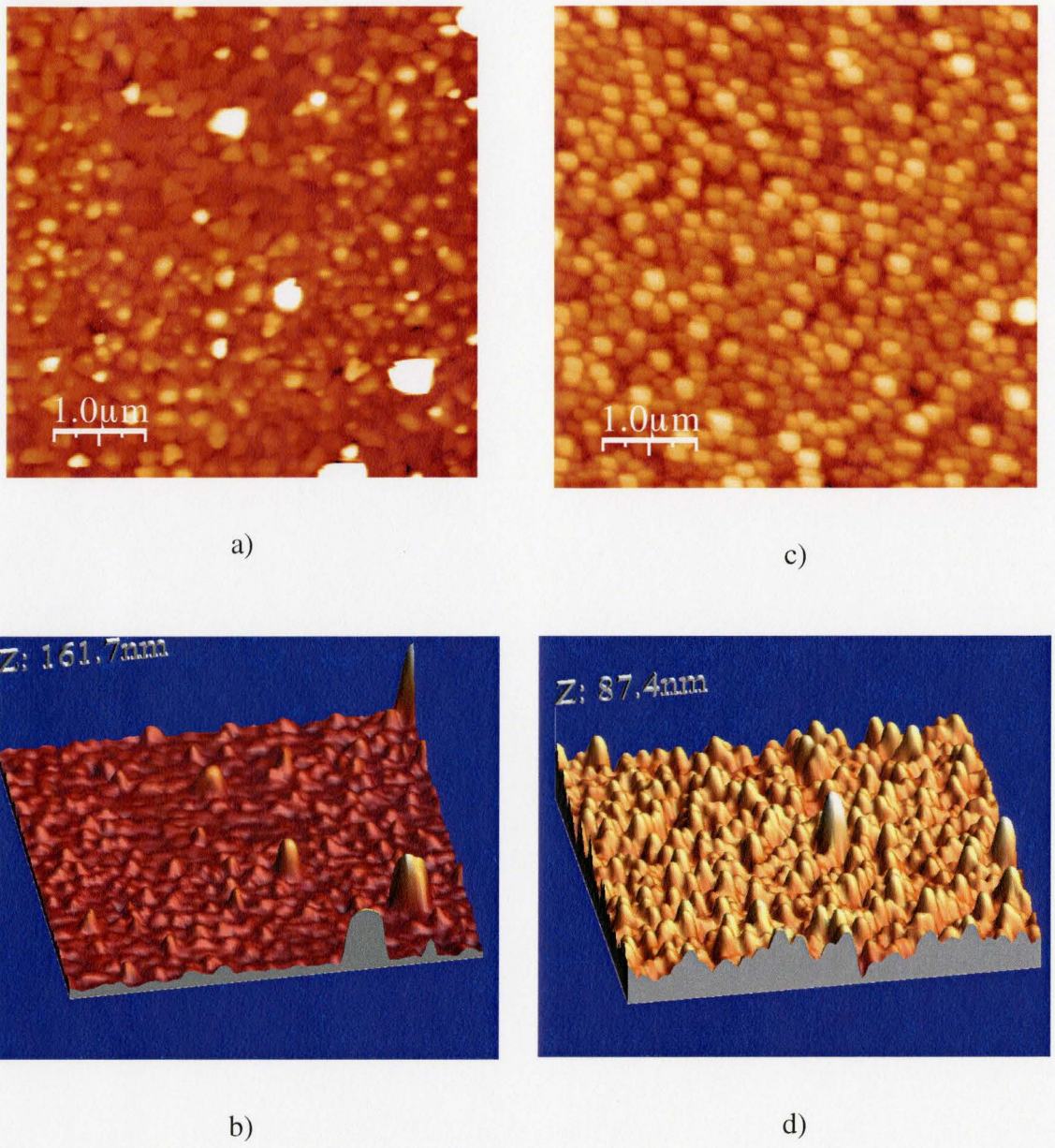

Figure 34: Topographical AFM image of a) b) (001) and c) d) (111) oriented PMN-0.35PT

Examination of thin films oriented in the (001) and (111) in piezoresponse mode revealed differences in the samples beyond growth orientation. In Figure 35, a (001) oriented sample, there appears to be no evidence of contrast in the piezoresponse image

beyond artifacts due to electrostatic forces derived from surface charge. This is as expected due to the electrostrictive nature of PMN as a bias voltage must be applied in order to observe the piezoelectric effects.

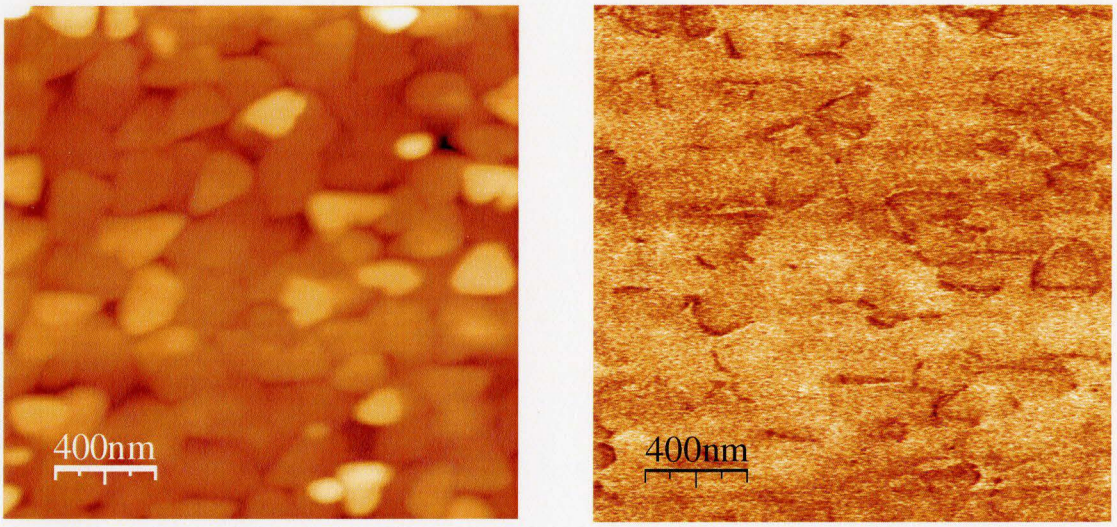

a) b)

Figure 35: AFM image of PMN-PT deposited in (001) orientation a)topography and b) is the associated piezoresponse image

However, in Figure 36 the images show that there is piezoresponse contrast, although no bias had been applied to the structure. There are numerous areas of contrast in Figure 36 b) indicating localized piezoelectric effect. Comparison of the topographic image in Figure 36 a) to its piezoresponse image shows that the piezoelectric effect is located entirely within the grains and in some adjacent grains. It was also found that when a field of 1V was applied to other areas of the film there was no evidence of induced polarization. Given that the film thickness was 50 nm this is equivalent to a field of approximately 200 kV/cm which greatly exceeds the typical coercive field of 25-30

kV/cm. Self-polarization within relaxor films has been previously observed by Kholkin et al[62] and later Kighelman[63] and Shvartsman et al[60]. The behavior, as observed in the films of this study, was found to develop only in select grains or in agglomerates of grains. Although, localized piezoelectric response, self polarization, and increased coercive field have been linked to numerous sources including grain size, compositional inhomogeneities, and strain and have been exhibited by similar systems including PMN-0.35PT.[60, 61,63]

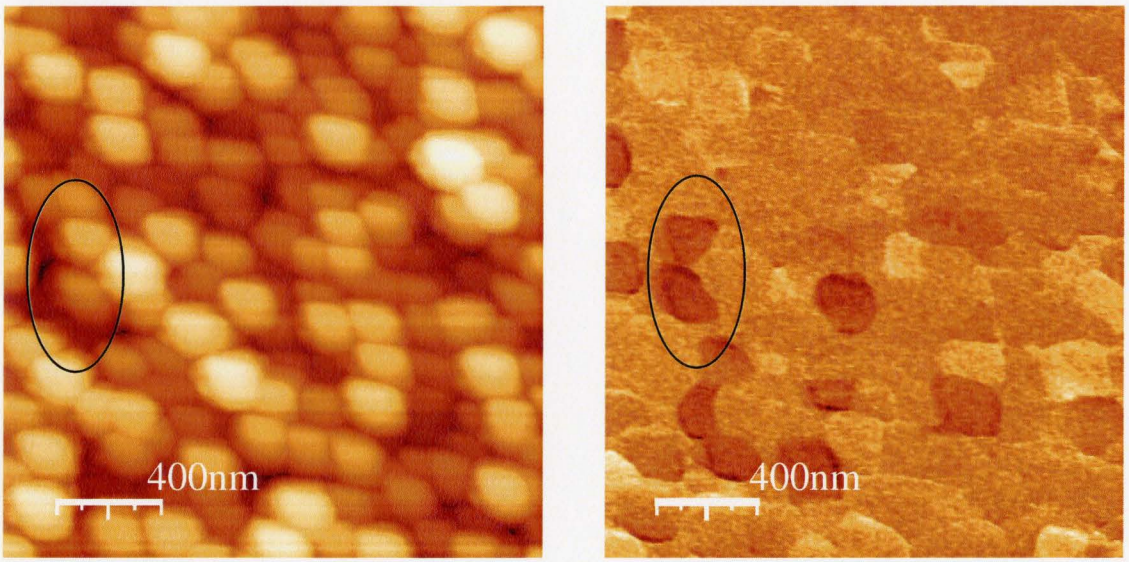

Figure 36: AFM image of PMN-PT deposited in (111) orientation a)topography and b) is the associated piezoresponse image

The effect of grain size in bulk ceramics as well as thin films and its effect on ferroelectricity has been well documented. Shvartsman et al[60] completed study on the effect of grain size in PMN-0.65PT and found that there was a linear relationship between the grain size and effective piezoelectric coefficient in thin films with remanent

polarization increasing with grain sizes from 100 - 450 nm. The average grain size in the thin film is approximately 200 nm which is within the dimensions required for a stable remnant piezoelectric coefficient. Assuming the composition across the film is uniform, the self polarization of the grains indicates that there is an inhomogeneous distribution of local internal electric fields within the film. This is deduced given that a bias field is required for the piezoelectric effect in relaxors[60]. However, if compositional inhomogeneites were introduced by deposition or localized ordering from diffusional processes, grains composed entirely of $PbTiO_3$, a strong normal ferroelectric may be possible also resulting in the observed piezoelectric response. Compositional investigation of individual grains which show piezoelectric response would be difficult if not impossible though, as locating the grain would pose a challenge as would maintaining their structure and environment during sample preparation.

In addition to the examination of the piezoelectric response of these materials the bottom electrode should have allowed the measurement of the dielectric constant and hysteresis loop by flat plate capacitor techniques. A difficulty arose in performing this series of experiments as the films had a significant leakage current and the many of the electrodes were short circuited due to porosity within the films. This was unexpected as the films should have a significant dielectric constant and be of sufficient thickness to avoid these effects. Cross-sectional samples were made of these films and investigated once again with TEM.

4.2.2 Microstructural Characterization

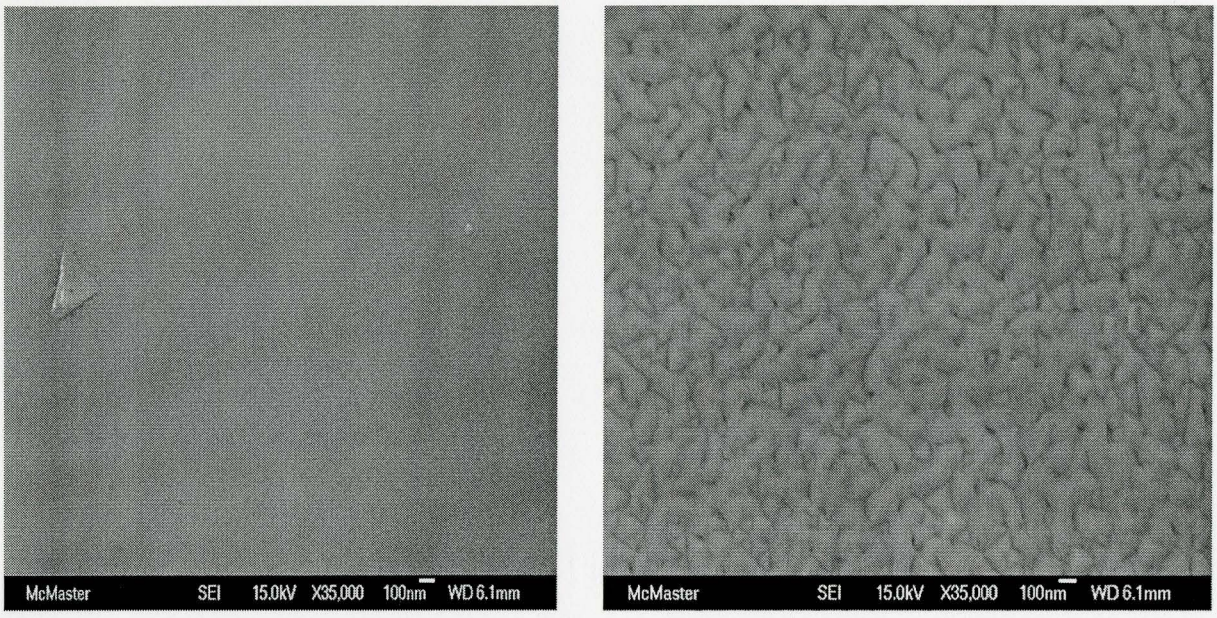

a) b)

Figure 37: SEM Micrograph of PMN-PT surface in a) (100) orientation and b) (111) orientation (Rob Hughes)

Based on the previous success of single layer PMN-PT deposition it was believed that completing a multilayer deposition under similar conditions would produce good quality films. The scanning probe microscopy and scanning electron microscopy (Figure 37) of the films proved otherwise and therefore a TEM investigation into the morphology of the films was carried out.

Examination of the sample in Figure 38 from the bottom up shows that the $MgAl_2O_4$ substrate does not appear to have any qualitative differences from that in the single layer samples.

In the $BaNb_{0.5}Ti_{0.5}O_3$ (BTN) layer there is evidence of a columnar structure. The columnar structure was investigated further and found to be quite prevalent in perovskites deposited by pulsed laser deposition. Consequently, due to the columnar nature of the electrode layer the probability of single crystal deposition on further layers significantly decreases.

The diffusion buffer layer between the $BaNb_{0.5}Ti_{0.5}O_3$ and PMN-0.35PT layer consists of $MgAl_2O_4$ once again. It is evident that, qualitatively speaking, the morphology of the layer is quite different that of the substrate. The deviation from single crystallinity is due to strain and dislocations introduced by growth on the BTN electrode as indicated by the significant contrast variation and evidence of grain boundaries.

Finally, the PMN-PT is clearly polycrystalline as shown in the bright field TEM cross section of Figure 38 with some separation between the grains. The phase development for PMN-0.35PT is known to depend on the lattice mismatch and quality of the substrate layer. Therefore, the poly-crystalline nature of the film can be entirely attributed to the layers below.

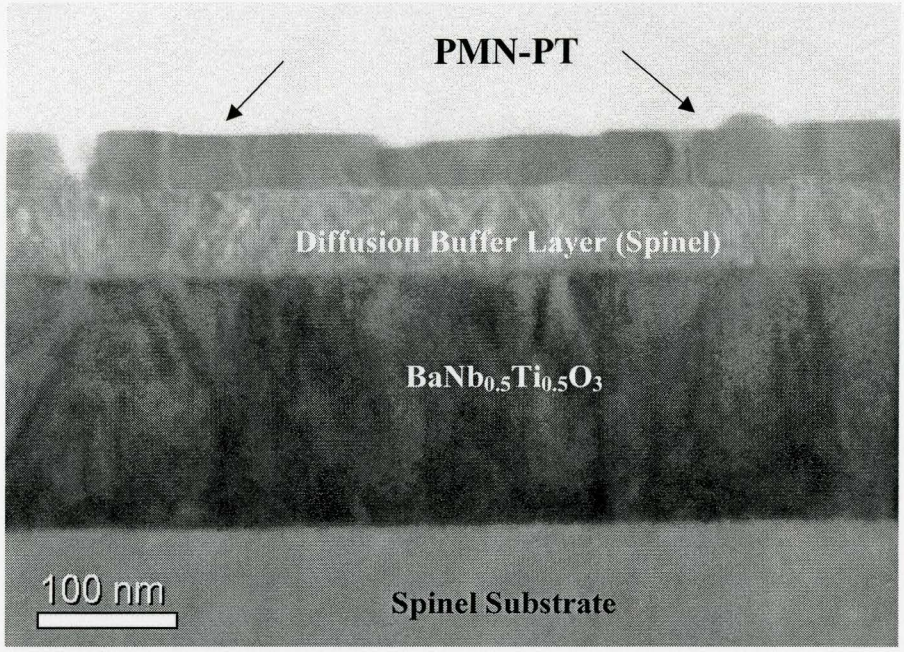

Figure 38: TEM cross-section of three layer heterostructure

The grain structure as shown in Figure 39 is an in plane rotation. The columnar growth mode is often seen during pulsed laser deposition when reorganization of the deposited layer cannot occur due to either low temperature or high frequency deposition[64]. It has also been directly observed in $BaTiO_3$ by Dey et al in films deposited by pulsed laser deposition and by Streiffer et al[65] in films deposited by metal orgainic chemical vapor deposition and attributed to tension in the film and a thickness dependency[66]

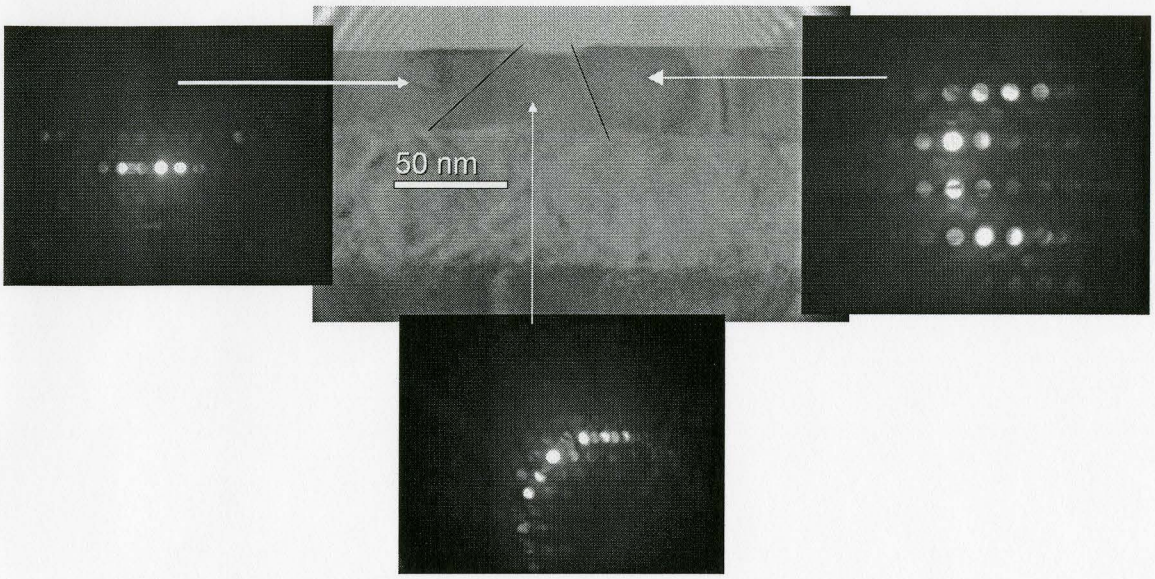

Figure 39: TEM Cross-section of PMN-0.35PT layer with associated CBED patterns

5 Conclusions

5.1 Summary

In this thesis the dielectric properties of single crystal PMN-0.35PT relaxor thin films were measured using interdigital capacitors and related to the microstructural properties by both TEM and piezoresponse microscopy for the first time.

It was found that using interdigital dielectrometry and Maxwell FEM the dielectric constant for the thin film ranged from 561 – 799 at 1kHz and 518 – 746 at 100kHz when the temperature was varied from 273-473K. Additionally, the temperature dependence of the dielectric maximum (T_m) is higher than previously reported at approximately 420K. The thin films displayed a typical relaxor ferroelectric behavior with a broad diffuse dielectric maximum. The reduction in dielectric maximum, when compared to values previously reported in literature, may be attributed to tensile strain imposed by the substrate $MgAl_2O_4$. This is despite fact that the lattice mismatch between the substrate and thin film, for the single layer samples, was smaller than in any previous publications. It is also believed that interdigital dielectrometry measurements were the first ever completed on thin film PMN-0.35PT with excellent film morphology as demonstrated in the TEM images for the single layer samples. Interdigital dielectrometry was also completed on both ceramic and single crystal samples of PMN-PT with good results establishing interdigital dielectrometry as a viable method for dielectric evaluation of thin films.

Piezoresponse microscopy and transmission electron microscopy have shown that regardless of the lattice mismatch within the heterostructure, it is difficult to produce high quality films of PMN-0.35PT with a $BaNb_{0.5}Ti_{0.5}0_3$ bottom electrode. The propensity for columnar growth of $BaNb_{0.5}Ti_{0.5}0_3$ establishes an environment for polycrystalline growth drastically reducing the probability of single crystal growth in subsequent layers. Additionally, piezoresponse microscopy allowed the observation of self polarization in PMN-0.35PT within the polycrystalline films which is in agreement with observations of previous researchers.

5.2 Recommendations for Future Work

As with all research projects it often seems that for every interesting result obtained many more topics for future work are discovered. This is especially true in the case of thin film ferroelectric materials as new applications are constantly being developed. Several suggestions for future research are proposed below:

- Examine and evaluate PMN-PT across a variety of substrates in order to establish an experimental misfit/dielectric constant phase diagram and compare with its thermodynamic counterpart
- Investigate changes in dielectric properties of the thin films with different substrate orientations
- Develop a method for producing free standing ferroelectric films in order to negate the biaxial tension imposed by the substrate material.
- Develop alternative bottom electrode materials which may be lattice tuned to the particular application

References

[1] Heartling, G; "Ferroelectric Ceramics: History and Technology" *J. Am. Ceram Soc.* **82 [4]** 797-818. , 1999.

[2] "An American National Standard IEEE Standard Definitions of Terms Associated With Ferroelectric and Related Materials" *IEEE Trans. Ultrasonics, Ferroelectrics, and Frequency Control* **50** 12, 2003.

[3] Jaffe, B., Cook, W.R., Jaffe, H., *Piezoelectric Ceramics.* Marietta, OH: R.A.N. Publishers, 1971

[4] G.A. Smolenskii and A.I. Agranovskaya, "Dielectric Polarization of a Number of Complex Compounds," *Sov. Phys.-Solid State (Eng. Trans.).* **1** 10 (1960): 1427.

[5] Cross, L.E.. "Relaxor ferroelectrics." *Ferroelectrics* 76.3 (1987):241.

[6] Tian-Ling Ren, Hong-Jin Zhao, Li-Tian Liu, Zhi-Jian Li, "Piezoelectric and ferroelectric films for microelectronic applications" *Materials Science and Engineering* B99 (2003):159.

[7] Franco Jona and G. Shirane; Ferroelectric Crystals Pergamon Press, 1962: New York pg 2

[8] Sawyer C.B., T ower C, . H., *Phys. Rev.,* 35,(1930):269.

[9] D. Damjanovic, "Ferroelectric, dielectric and piezoelectric properties of ferroelectric thin films and ceramics" *Rep. Prog. Phys.* **61**, (1998):1267.

[10] Fousek J., Janovec, V.,"The Orientation of Domain Walls in Twinned Ferroelectric Crystals" *Jounal of. Applied. Physics.* **40**, (1969):135.

[11] Alpay, S. and Roytburd, A. "Thermodynamics of polydomain heterostructures III. Domain Stability Map" *Journal of Applied Physics* **83** 9 (1998): 4714-4723.

[12] Park S.E., Shrout T.; "Characteristics of Relaxor-Based Piezoelectric Single Crystals for Ultrasonic Transducers" *IEEE Trans on Ultrasonics, Ferroelectrics and Frequency Control.* **44** 5 (1997):1140.

[13] Park S.E., Shrout T "Ultrahigh strain and piezoelectric behavior in relaxor based ferroelectric single crystals" *Journal of Applied Physics.* **82** 4 (1997):1804.

[14] Bokov, A.A.. "Giant electrostriction and stretched exponential electromechanical relaxation in $0.65Pb(Mg_{1/3}Nb_{2/3})O_3$-$0.35PbTiO_3$ crystals." *Journal of applied physics* **91**.10 (2002):6656.

[15]Choi,S.W. Shrout, T.R.; Jang, S.J.; Bhalla, A.S. "Morphotropic phase boundary in $Pb(Mg_{1/3}Nb_{2/3})O_3PbTiO_3$ system." Materials letters *8*.6 (1989):253.

[16] "An American National Standard IEEE Standard Definitions of Terms Associated With Ferroelectric and Related Materials" *IEEE Trans. Ultrasonics, Ferroelectrics, and Frequency Control* **50** 12, (2003).

[17] Tantigate, C., Lee, J. Safari, A. "Processing and properties of $Pb(Mg_{1/3}Nb_{2/3})O_3$-$PbTiO_3$ thin films by pulsed laser deposition" *Applied Physics Letters* **66,** (1995):1611.

[18] Maria, J.P. Hackenberger, W., Trolier-McKinstry., "Phase development and electrical property analysis of pulsed laser deposited $Pb(Mg_{1/3}Nb_{2/3})O_3$-$PbTiO_3$ (70/30) epitaxial thin films" *Journal of Applied Physics* **84** 9, (1998):5147.

[19] Udayakumar, K.R.. "Polarization reversal and high dielectric permittivity in lead magnesium niobate titanate thin films." Applied physics letters 60.10 (1992):1187.

[20] Wasa., K et al., "Structure and Ferroelectric Properties of Single Crystal PMNT Thin Films" *Integrated Ferroelectrics* **70** (2005):131.

[21] Viehland D, Li J. F., Jang S.J., Cross L.E., and Wuttig M." Dipolar-glass model for lead magnesium niobate" *Phyical Reviews B* **43** 10 (1991): 8316.

[22] Glinchuck, M.D., "Relaxor ferroelectrics: from Cross superparaelectric model to random field theory" *British Ceramic Transactions* **103** 2 (2004): 76.

[23] Smith,H. M., Turner, A.F.,"Vacuum Deposited Thin Films using a ruby laser" *Applied Optics.* **4,** (1965): 147.

[24] Chrisey D.B. and Hubler G.K., **Pulsed Laser Deposition of Thin Films,** 1994. New York:John Wiley and Sons Inc.

[25] Pertsev et al. "Ferroelectric thin films grown on tensile substrates: Renormalization of the Curie-Weiss Law and Apparent absence of ferroelectricity" *Journal of Applied Physics*, **85** 3 (1999):1698.

[26] Maria, J.P., et al. "Thickness, Strain and Temperature-Dependant Properties of Barium Strontium Titanate Thin Films" *IEEE* (2002):151.

[27] Wasa et al, "Thin Film Effects in the Ferroelectric $PbTiO_3$" *IEEE Ultrasonics Symposium* (1999).

[28] Chandra, P et al "Scaling of the Coercive Field with Thickness in thin Film Ferroelectrics" *Ferroelectrics* **313** (2004): 7.

[29] Pertsev et al. "Effect of Mechanical Boundary Conditions of Phase Diagrams of Epitaxial Ferroelectric Thin Films" *Physical Review Letters*, 80 9 (1998):1988.

[30] Maria, J.P., et al. "Thickness, Strain and Temperature-Dependant Properties of Barium Strontium Titanate Thin Films" *IEEE* (2002):151.

[31] Wasa et al, "Thin Film Effects in the Ferroelectric $PbTiO_3$" *IEEE Ultrasonics Symposium* (1999).

[32] N. Tesla "Electric condenser" U.S. Patent 464 667, 1891.

[33] Mamishev, A et al. "Interdigital Sensors and Transducers" *Proceedings of the IEEE.* **92** 5 (2004): 808.

[34] Farnell, G.W. et al. "Capacitance and Field distributions for Interdigital Sufacewave Transducers." *IEEE Trans Sonics Ultrasonics*, SU-17, 3, (1970): 188.

[35] Prume, K.. "Finite element simulations of interdigital electrode structures on high permittivity thin films." *Integrated ferroelectrics* **32**.1 (2001):755.

[36] Wei, John S.. "Distributed Capacitance of Planar Electrodes in Optic and Acoustic Surface Wave Devices" *IEEE journal of quantum electronics* **13**.4 (1977):152.

[37] Gevorgian, S. "CAD Models for Multilayerd Substrate Interdigital Capacitors" *IEEE Trans. On Microwave Theory and Techniques.* **44** 6 (1996): 896.

[38] Igreja, R., Dias, .C.J., "Analytical evaluation of the interdigital electrodes capacitance for multi-layered structure" *Sensors and Actuators A* **112** (2004): 291.

[39] F. Saurenbach and B.D. Terris, "Imaging of ferroelectric domain walls by force microscopy" *Applied Physics Letters.* **56** 17, (1990): 1703.

[40] Hong et al, "Principle of ferroelectric domain imaging using atomic force microscope" *Journal of Applied Physics* **89** 2 (2001): 1377 .

[41] H. Birk, J. Glatz-Reichenbach, Li Jie, E. Schreck, and K. Dransfeld, "The local piezoelectric activity of thin polymer films observed by scanning tunneling microscopy" *Journal of Vacuum Science and. Technology. B* **9**, pt.2, (1991): 1162.

[42] K. Franke, J. Besold, W. Haessler, and C. Seegebarth, *Surf. Sci. Lett.* **302,** L283 (1994).

[43] T. Hidaka, T. Maruyama, M. Saitoh, N. Mikoshiba, M. Shimizu, T. Shiosaki, L.A. Wills, R. Hiskes, S.A. Dicarolis, and J. Amano "Formation and observation of 50 nm polarized domains in $PbZr_{1-x}Ti_xO_3$ thin film using scanning probe microscope" *Applied Physics Letters.* **68**, 17 (1996): 2358.

[44] A. Gruverman, O. Auciello, and H. Tokumoto, "Nanoscale investigation of fatigue effects in $Pb(Zr,Ti)O_3$ films" *Applied Physics Letters.* **69**, 21 (1996): 3191.

[45] A. Gruverman, H. Tokumoto, S.A. Prakash, S. Aggarwal, B. Yang, M. Wuttig, R. Ramesh, O. Auciello, and T. Venkatesan, "Nanoscale imaging of domain dynamics and retention in ferroelectric thin films" " *Applied Physics Letters* **71** 24, (1997): 3492.

[46] L.M. Eng, H.J. Güntherodt, G. Rosenman, A. Skliar, M. Oron, M. Katz, and D. Eger, "Nondestructive imaging and characterization of ferroelectric domains in periodically poled crystals" *Journal of Applied Physics* **83** 11 (1998): 5973.

[47] L.M. Eng, M. Abplanalp, and P. Günter, "Ferroelectric domain switching in tri-glycine sulphate and barium-titanate bulk single crystals by scanning force microscopy "*Applied. Physics. A* **66** (1998): S679.

[48] V. Likodimos, X.K. Orlik, L. Pardi, M. Labardi, and M. Allegrini, "Dynamical studies of the ferroelectric domain structure in triglycine sulfate by voltage-modulated scanning force microscopy" *Journal of Applied Physics* **87 1** (2000): 443.

[49] A.L. Kholkin, C. Wütchrich, D.V. Taylor, and N. Setter, "Interferometric measurements of electric field-induced displacements in piezoelectric thin films" *Review of Scientific Instruments.* **67** 5, (1996): 1935.

[50] Durkan, C., Welland, M.E., "AFM characterization of domain structure of ferroelectric TGS crystals on a nanoscale" Ultramicroscopy **82** (2000): 142.

[51] Thesis, Zhouying Chen, "Transmission Electron Microscopy Characterization (TEM) of Relaxor Ferroelectric Single Crystals and Thin Films" McMaster University (2004).

[52] Maeder, T., Sagalowicz, L., Muralt, P., "Stabilized Platinum Electrodes for Ferroelectric Film Deposition using Ti, Ta and Zr Adhesion Layers" *Jpn J. Applied Physics.* **37** (1998): 2007.

[53] Wang, Y., Chong, Y.L., Cheng, H.L.W., Chan, C.L. "Dependence of Capacitance on electrode configuration for ferroelectric films with interdigital electrodes" *Microelectronic Engineering* **66** (2003): 880.

[54] Wasa., K et al., "Structure and Ferroelectric Properties of Single Crystal PMNT Thin Films" *Integrated Ferroelectrics* **70** (2005): 131.

[55] Tantigate, C., et al "Processing and properties of $Pb(Mg_{1/3}Nb_{2/3})O_3$–$PbTiO_3$ thin films by pulsed laser deposition" *Applied physics letters* **66** 13 (1995):1611.

[56] Donnelly et al. "Dielectric and electromechanical properties of PMN-PT thin films grown by PLD" *Journal of Applied Physics* **93** 12 (2003): 9924.

[57] Kumar, Pawan. "Dielectric, ferroelectric and pyroelectric properties of PMNT ceramics." *Physica. B, Condensed matter* **371** 2 (2006):313.

[58] Krupanidhi, S.B., Laha, A., "Investigation of Relaxor Behavior in $Pb(Mg_{1/3}Nb_{2/3})O_3$–$PbTiO_3$ Thin Films" *Ferroelectrics* **306** (2004): 17.

[59] Pertsev et al. "Ferroelectric thin films grown on tensile substrates: Apparent absence of ferroelectricity" *Journal of Applied Physics*, **85** 3 (1999): 1698.

[60] Shvartsman, V.V.et al. "Local hysteresis and grain size effect in $Pb(Mg_{1/3}Nb_{2/3})O_3$–$PbTiO_3$ thin films." *Applied physics letters* **81** 1 (2002):117.

[61] Shvartsman, V.V.. "Relaxation of induced polar state in relaxor $Pb(Mg_{1/3}Nb_{2/3})O_3$ thin films studied by piezoresponse force microscopy." *Applied physics letters* **86** 22 (2005):222907.

[62] Kholkin, A., Tantigate, G., Safari, A. "Electromechanical properties of PMN-PT thin films prepared by pulsed laser deposition technique." *Integrated ferroelectrics* **22** 1 (1998):515.

[63] Kighelman, Zian. Damjanovic, D., Setter, N. "Electromechanical properties and self-polarization in relaxor $Pb(Mg_{1/3}Nb_{2/3})O_3$ thin films." Journal of applied physics **89** 2 (2001):1393.

[64] Blank, D.H.A, et al "Imposed layer by layer growth by pulsed laser interval deposition" *Applied Physics A 69 S17-S22 (1999)*

[65] Streiffer, S.K. et al "Ferroelectricity in thin films: The dielectric respons of fiber-textured $(Ba_xSr_{1-x})Ti_{1+y}O_{3+z}$ thin films grown by chemical vapor deposition" *Journal of Applied Physics* **86** 8 (1999): 4565.

[66] Dey, Sandwip K.. et al "Microstructure evolution of pulsed laser-Deposited (Ba, Sr)TiO_3 films on MgO for microwave applications." *International journal of applied ceramic technology* **2** 1 (2005):59.